Extended P-I diagram method

Chernin, Leon; Vilnay, Margi; Cotsovos, Demetrios M.

Published in:
Engineering Structures

DOI:
10.1016/j.engstruct.2020.111217

Publication date:
2020

Licence:
CC BY-NC-ND

Document Version
Peer reviewed version

Extended P-I Diagram Method

Leon Chernin[1#], Margi Vilnay[1], Demetrios Cotsovos[2]

[1] School of Science and Engineering, University of Dundee, Dundee, UK

[2] School of Energy, Geoscience, Infrastructure and Society, Heriot Watt University, UK

[#]Corresponding author: email l.chernin@dundee.ac.uk, tel. +44(0)1382 384922, fax +44(0)1382 384389

Abstract

The pressure-impulse (P-I) diagram method is used in practice (for civilian and military applications) for predicting the level of damage sustained by structures when subjected to blast loads and for assessing the imposed loading regime. Each P-I curve is associated with a certain structural configuration as well as a specific form of blast load and level of damage sustained. When assessing the effect of different parameters (associated with the form of the imposed load and the design of the structure considered) on structural performance, a series of new P-I curves need to be derived. This paper presents an extended P-I diagram method, which is based on derivation of complementary diagrams that can define the effect of two parameters (e.g., the level of axial loading imposed onto a column and the level of damage sustained) on the quasi-static and impulsive asymptotes, thus governing the positions of P-I curves in the diagram plane. The extended P-I diagram method is presented in dimensional and normalised forms. The dimensional form simplifies the derivation of new P-I curves, while the normalised form simplifies the procedure adopted for assessing the behaviour of a certain structure when subjected to a new set of loads. The application of the proposed method is demonstrated in both forms using a typical reinforced concrete (RC) column subjected to a blast load. The column is modelled using finite element analysis capable of accounting for the nonlinear behaviour of concrete and steel. A novel method is proposed for material modelling of concrete. The new material model is validated at both material and structural levels against relevant experimental data. P-I diagrams are initially derived for the axially unloaded column, while complementary diagrams are derived for the column loaded by different axial forces. The framework of the extended P-I diagram method employed for the derivation of new P-I curves and the assessment of

the level of damage sustained by the column when subjected to different loading conditions is provided herein.

Keywords: P-I Diagram Method, Damage, Blast, Reinforced Concrete, Column, Finite Element Modelling

1. Introduction

Loss of structural integrity (resulting in partial or full collapse) can occur when structures are subjected to blast loads caused either by accidental (e.g. the Ronan Point collapse in London in 1968, the Stockline factory blast in Glasgow in 2004, the Piper Alpha offshore oil rig disaster in 1988, the Deepwater Horizon offshore oil rig explosion in 2010, Petrobras Brazil offshore gas rig explosion in 2015) or deliberate (e.g. the Oklahoma City bombing in 1995, London bombings in 2005) explosions. Explosions can cause damage to structural components, the collapse of walls, the generation of fragments/debris, the blowing out of large expanses of windows and the shutting down of critical safety-related systems/controls. As a result, the analysis and the design of a wide range of civil, industrial and military structures can be highly influenced by the consideration of such extreme events. Additionally, it is often important to be able to quickly but realistically assess the residual load-carrying capacity of a structure in the aftermath of an explosion in order to determine its survivability or enable the evacuation of injured occupants and allow access to critical services/controls.

Pressure-impulse (P-I) diagrams can be used for developing an effective and practical method for the preliminary assessment of structures damaged by explosions, e.g., [1-7]. They provide explicit visual information concerning the loading regime and the post-blast (residual) condition of a structure. This method can also be adopted for assessing the residual load-carrying capacity and the survivability of a structure after an explosion event. P-I diagrams are usually developed for a single structural element, e.g., beam, column, wall, slab [7], although the application of P-I diagrams to frames [8] and even whole buildings [9] is possible. Each P-I curve is built for a unique combination of loads acting on a specific

structure and for a specific level of damage [7]. The P-I diagrams are sensitive to variations in the design parameters of the structure considered and load time-history applied. This sensitivity can partially be considered by building additional P-I curves reflecting the effect of a certain parameter [1, 3, 4, 6, 10-16], using P-I bands [3], building three dimensional diagrams [3, 10, 17-20] and applying various normalisation techniques [4, 10, 15, 21-27].

The work presented herein sets out to extend and enhance the applicability of the P-I diagram method by building a series of complementary diagrams. These diagrams separately describe the effects of a specific design or loading parameter on structural response under impulsive and static (or quasi-static) loading regimes. The extended P-I diagram method can be applied in dimensional and normalised forms. The dimensional form can be used for the rapid derivation of new P-I curves, whereas the normalised form can simplify the application of the method by eliminating the need for derivation of additional P-I curves. The application of the proposed method is demonstrated herein for the case of an RC column initially subjected to a certain level of axial loading and subsequently to a blast load. The behaviour of the subject structure is predicted numerically through the use of a nonlinear finite element method software – Abaqus [28]. A 3D numerical model, representing the structure at hand, is initially created. A novel method is employed to describe concrete material behaviour, where the brittle cracking model built-in in Abaqus [28] is extended using user subroutines to include nonlinear behaviour in compression [29]. The behaviour of the reinforcing steel bars is described using classic plasticity theory. Numerous computational simulations were performed, during which the column was subjected initially to a predefined axial force and subsequently to a lateral blast load. Based on the predictions obtained complementary diagrams were then derived and presented in the form of axial force-impulse and axial force-pressure curves. It is necessary to note that the approach proposed herein builds upon previous research carried out on the topic, e.g. [1], [14], [24]–[27], and represents a step towards the visual interpretation of the effects of various structural and loading parameters on certain key characteristics of structural response. This is

especially important in engineering practice and convenient for implementation in relevant standards and design codes as well as for educational purposes.

2. Extended P-I diagram method

A typical form of the P-I curve is very close to a rectangular hyperbola (see Figure 1). Note that Figure 1 presents schematically a normalised P-I diagram, where I and I_{cr} are the applied and critical impulses, and P and P_{cr} the applied and critical pressures. Each point of the P-I curve is defined by a limit state function G representing structural damage, e.g., [28]–[31]. G can be expressed as

$$G(I,P) = \lambda/\lambda_{max} \tag{1}$$

where λ represents the failure criterion, that can be potentially associated with the peak deflection exhibited at a specific (critical) point along the span of a structural element [12, 22-24], or the residual axial load-carrying capacity [1, 6, 17]. $G \geq 1$ corresponds to the state of structural failure. G can also represent structural survivability or safety, if the form of Eq. (1) is changed to $G(I,P) = 1 - \lambda/\lambda_{max}$, e.g., see [24, 30].

A typical P-I curve can be generally divided into a vertical asymptote, a hyperbolic curve and a horizontal asymptote as depicted in Figure 1. These three parts represent the (I) impulsive, (II) dynamic and (III) static or quasi-static loading regimes. The vertical asymptote is called impulsive while the horizontal asymptote can be static or quasi-static depending on the blast load rise time [7, 12]. In this paper, a zero-rise time is considered; therefore, the horizontal asymptote becomes quasi-static.

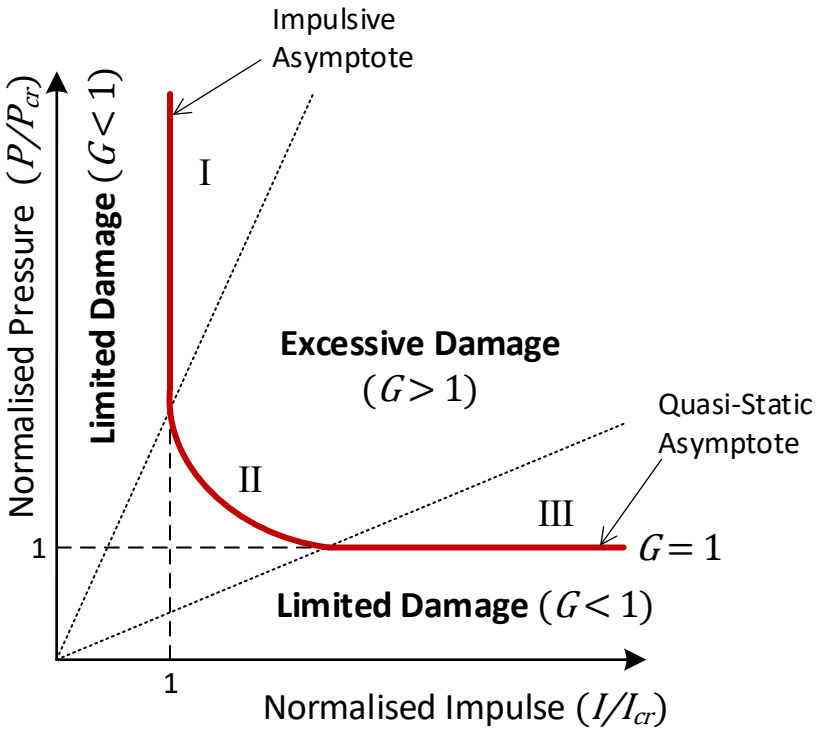

Figure 1. Schematic normalised P-I diagram

The position of each P-I curve is controlled by the impulsive and quasi-static asymptotes. The positions of the impulsive and quasi-static asymptotes are influenced by a range of parameters associated with the design of the structure considered as well as the imposed loading and boundary conditions (see Figure 2). Attempts to express the influence of various parameters on the impulsive and quasi-static asymptotes have been made in previous research studies, e.g., [1], [14], [24]–[27], using least-square curve fitting. Alternatively, the variation in the positions of the asymptotes can be graphically described by complementary *Parameter-Impulse* and *Parameter-Pressure* diagrams, where 'Parameter' is any structural or loading parameter selected. The application of the complementary diagrams is schematically shown in Figure 2 using a Force (N) as the 'Parameter' and therefore a series of complementary Force-Impulse (N-I) and Force-Pressure (N-P) diagrams are derived. Note that Figure 2 presents schematically the normalised P-I, N-I and N-P diagrams, where N and N_{cr} are the applied and critical forces, I and I_{cr} the applied and critical impulses, and P and P_{cr} the applied and critical pressures. As can be seen, the N-P diagram controls the positions of the quasi-static asymptote, while the N-I diagram controls the impulsive asymptote. The

N-P and N-I relationships can be linear or nonlinear depending on the complexity of structural system considered.

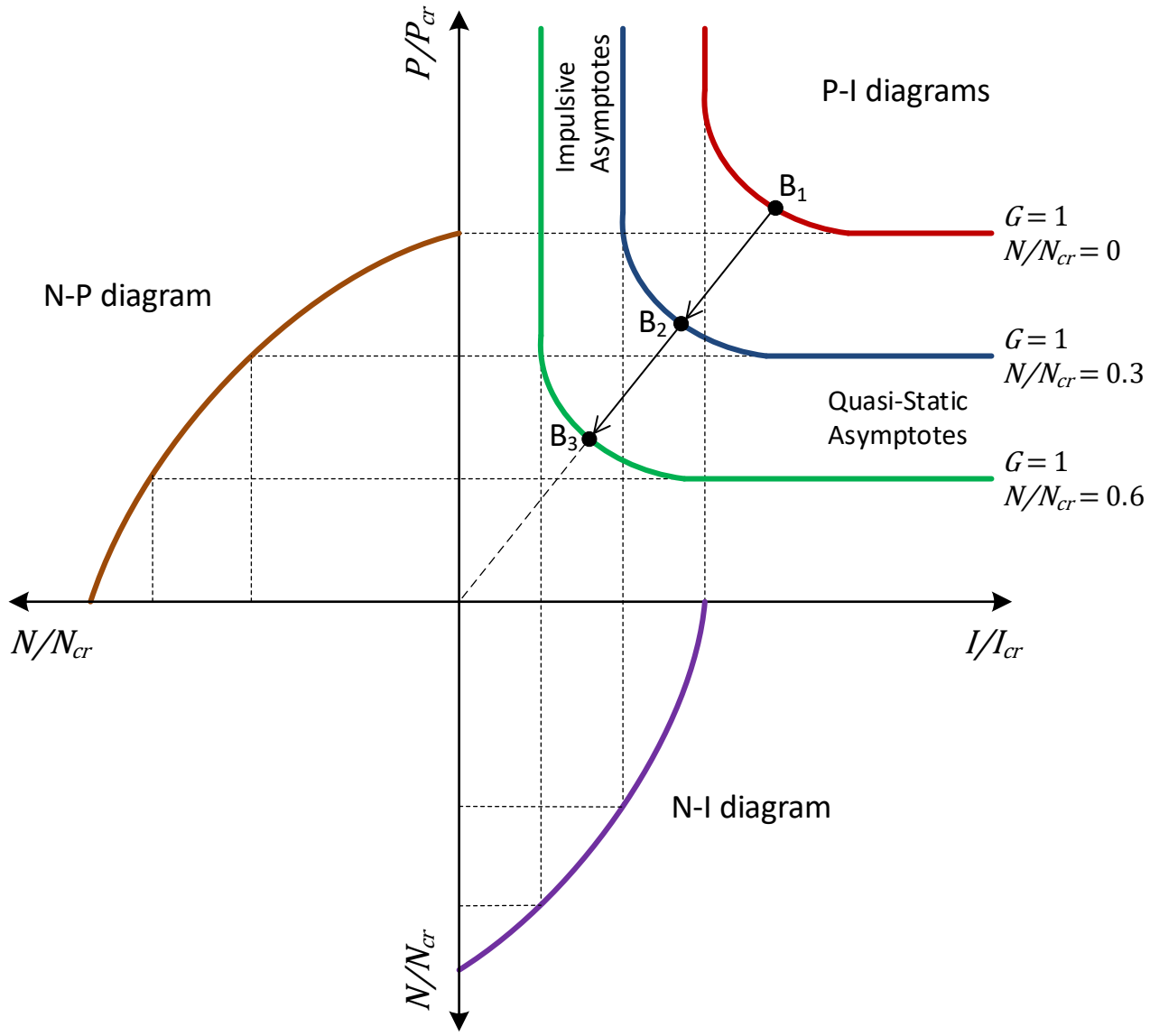

Figure 2. Schematic normalised P-I, N-I and N-P diagrams

The extension of the P-I diagram method through the use of the complementary diagrams allows the consideration of the combined effect of two parameters on the P-I curve. For example, Figure 3 schematically illustrates the normalised N-I (and N-P) diagram constructed for different levels of axial force and damage. In this figure, N and N_{cr} are the applied and critical forces, I and I_{cr} the applied and critical impulses, and P and P_{cr} the applied and critical pressures. The degree of structural damage is defined using the limit state function in Eq. (1), when setting G = 0.1, 0.5 and 1.0, which corresponds to 10%, 50%

and 100% damage, respectively. It is necessary to note that the shape of both the N-I and N-P curves depends on the complexity of structural system analysed.

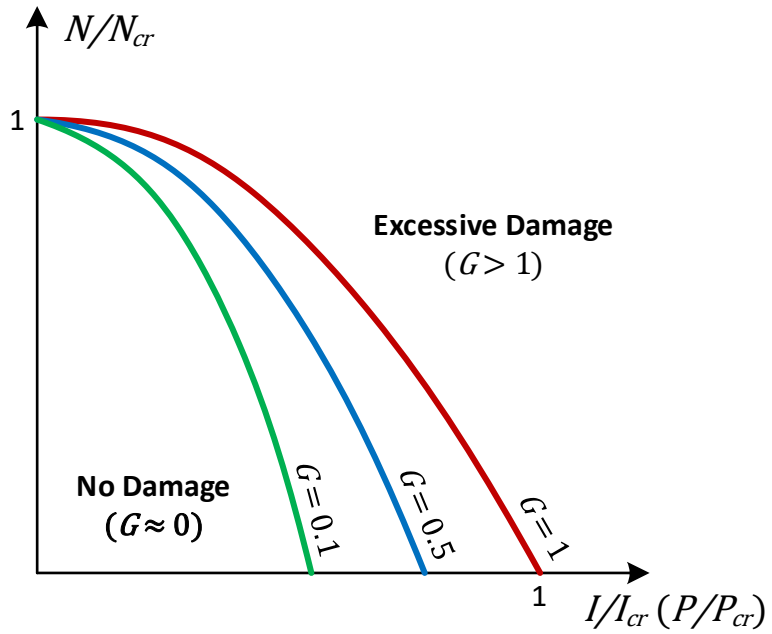

Figure 3. Extended N-I (N-P) diagram

Several published studies (e.g., [1, 6, 13, 17, 31, 32]) have proposed the use of nonlinear finite element analysis for determining the relationships for the impulsive and static asymptotes which depended on multiple structural parameters such as the longitudinal and transverse reinforcement ratio, geometry, the compressive strength of concrete, the exhibited deflections, etc. The proposed graphical approach can complement these studies by allowing the visual representation of the effects of various studied parameters on the exhibited structural behaviour.

The extended P-I diagram method is further introduced in dimensional and normalised forms. The dimensional approach can be applied for the derivation of additional P-I curves. When adopting the normalised approach, the derivation of additional curves can be avoided by derivation of a universal normalised P-I curve and mapping the blast load into the normalised P-I plane. This simplifies the application of the P-I diagram method. Additionally, the latter approach can be applied when assessing whether a structure reached a specific damage level.

2.1. Dimensional approach

In the dimensional approach, each new P-I curve can be generated by copying an existing P-I curve to a new position defined by the N-I and N-P diagrams and scaling the coordinates of each point on the curve along the axes. The scaling is carried out using the following scaling factors

$A_{I,new}/A_{I,old}$ along the *Impulse* axis

$A_{P,new}/A_{P,old}$ along the *Pressure* axis

where the subscripts *new* and *old* represent the new and old impulsive (A_I) and static (A_p) asymptotes. The presented approach assumes that the P-I curves generated for a structural system under scaled loads have the same basic shape, e.g., a rectangular hyperbola. This assumption is supported by the findings reported in [1, 11, 33, 34].

2.2. Normalised approach

The dimensional approach is no longer efficient when several structural states (corresponding, for example, to different levels of axial loading and damage) are being considered. In this situation, the normalised approach is more suitable. This approach requires an initial normalisation of the P-I diagram. The N-I and N-P diagrams can be used in either normalised or original forms. The normalised P-I diagram is obtained from the original diagram by scaling it along the coordinate axes using the following normalisation factors

$1/A_I$ along the *Impulse* axis

$1/A_p$ along the *Pressure* axis

A_I and A_P are defined using the N-I and N-P diagrams. The N-I and N-P diagrams are used to define the structural state (corresponding to different levels of axial loading and damage) through the normalisation factors. The three-diagram system can be used to assess whether a structure reached a specific structural

state (i.e. a specific damage level) after being subjected to a specific blast load. The algorithm employed for the assessment of the structural condition relatively to a defined level of damage can be summarised as follows:

1. N-I and N-P diagrams and at least one P-I diagram are derived.
2. The P-I diagram is normalised using corresponding normalisation factors $1/A_I$ and $1/A_p$.
3. A new structural state and a new blast load are selected for examination. This results in the selection of new values for $A_I$and A_p.
4. A blast load, described in terms of *I* and *P*, is normalised using the normalisation factors $1/A_I$ and $1/A_p$ corresponding to the examined structural state.
5. A point (I/A_I, P/A_p) corresponding to the normalised *I* and *P* is positioned on the normalised P-I diagram and the situation is assessed.

In this algorithm, the value of $A_I$and A_p, selected at Step 3, define the specific level of damage. The advantage of the normalised approach is that it eliminates the need to derive new P-I diagrams, as only one (universal) normalised P-I diagram is required. The assessment of a specific structural state can be carried out by mapping the values of *I* and *P* corresponding to a blast load onto the normalised P-I (i.e. $P/A_p - I/A_I$) plane using different values of $A_I$and A_p. Therefore, the normalised approach can quickly establish safe limits for combinations of structural and loading parameters during design of multiple typical structures.

3. Numerical simulation

Assessing the behaviour of reinforced concrete (RC) structural elements subjected to blast loads is a rather difficult task. It is usually achieved, either experimentally, through the use of sophisticated testing equipment, or numerically, by employing specialised nonlinear finite-element method (NLFEM) packages. Experimental investigations are expensive and hazardous and do not always yield measurements sufficiently accurate to provide a realistic description of the structural response. Additionally, the duration

of testing is extremely short (usually of the order of a few milliseconds), the loads generated are considerably greater by comparison to those imposed in the case of static testing and often result in explosive types of failure. The use of NLFEM packages can provide a more detailed description of the exhibited RC structural response in a more cost-efficient manner.

It has been established both experimentally [35-40] and numerically [11, 41-45] that RC structural response exhibits significant departures from that observed under equivalent static loading as certain thresholds of applied loading rate are surpassed. Such changes become more pronounced with increasing loading rates and intensities. The application of high-rate (e.g. blast) loading on RC structures results in the generation of stress waves, the propagation of which, within a heterogeneous material such as concrete, results in the development of a complex triaxial stress field [46]. This field is further accentuated by the cracking processes of concrete and the deflection of the waves on the developing cracks and on the boundaries of the structure [42, 43]. Hence, defining the response of RC structures under high-rate loading is a complex wave-propagation problem within a highly nonlinear medium. Abaqus is often used for modelling RC structures (e.g. [16]–[20]) and is capable of carrying out three-dimensional (3D) static and dynamic nonlinear finite element analysis. It incorporates a simple brittle model (termed “brittle cracking model”) in order to describe concrete material behaviour. The latter model is purpose-built for brittle materials the behaviour of which is dominated by tensile cracking [47]. This is largely true in the case of reinforced concrete (RC) flexural structural elements where cracks form due to the development of tensile strains within the concrete medium in the tensile region of the element considered. Such cracks gradually extend (into the compressive region) with increasing levels of applied loading, ultimately leading to structural failure and collapse. Another type of concrete failure is crushing under excessive compression loads, which is important for accurate description of the failure and post-failure mechanics of RC structures. In this paper, the brittle cracking model is extended to include a nonlinear compressive behaviour using a user subroutine.

3.1. Extended brittle cracking model

The brittle cracking model is built to work in Abaqus with the explicit time integration scheme [28]. It is an elastic cracking model with concrete between cracks considered as an isotropic linearly elastic material. In this model, the initiation and evolution of individual cracks is not tracked. Instead, a smeared crack method is utilised to model localised failure of the material (cracking). The constitutive calculations are independently performed at each material point of a finite element. The presence of cracks affects the stress and material stiffness associated with the material point. A simple Rankine criterion is used to detect crack initiation. Thus, a crack forms when the maximum principal tensile stress exceeds the tensile strength of the concrete. The crack surface is oriented in the direction normal to the maximum principal tensile stress. Once a crack is formed at a point, its orientation is stored for subsequent calculations. A new crack can form at the same point only in a direction orthogonal to the direction of an existing crack (i.e. fixed orthogonal crack model model). Cracks are modelled as irrecoverable. They may close and reopen but remain throughout the rest of the analysis. The sensitivity to the size of finite elements in the mesh introduced by the smeared crack method is eliminated using the Hillerborg's cohesive crack model [48]. This model relates tension strain softening to fracture energy of the material and the size of the finite element crossed by the smeared crack. The brittle behaviour of concrete in tension is described using the stress-displacement response rather than the stress-strain response. In this study, the stress-displacement curve has been obtained using FIB Model Code 2010 [49]. The effect of the amount of crack opening on the shear response of concrete is formulated using the shear retention model. In this model, the post-cracked shear stiffness is defined as a power function of the strain across an opening crack, reducing as the crack opens.

The elastic behaviour of the brittle cracking model in compression was transformed into a nonlinear behaviour of a damaged elasticity model, where the elastic modulus decreased as a function of the maximum compressive stress. This transformation was performed using the user subroutine VUSDFLD

[28], which allows the material properties to be redefined at a material point as a function of a field variable such as stress, strain, temperature, etc. The field variable is updated at each analysis step and the value of the relevant material property is recalculated. In this study, the nonlinear compressive behaviour of concrete is introduced into the brittle crack model by formulating the modulus of elasticity of concrete (E_c) as a function of strain (ε_c). To define the $E_c - \varepsilon_c$ function, the stress-strain ($\sigma_c - \varepsilon_c$) relationship describing the uniaxial compression behaviour of concrete is adopted from FIB Model Code [49]

$$\frac{\sigma_c}{f_{cm}} = -\frac{k\cdot\eta-\eta^2}{1+(k-2)\cdot\eta} \quad \text{for} \quad \varepsilon_c < \varepsilon_{c,lim} \tag{2}$$

where $\eta = \varepsilon_c/\varepsilon_{c1}$, ε_{c1} is the strain at the maximum compressive stress f_{cm}, $\varepsilon_{c,lim}$ is the strain at crushing of concrete in compression, $k = E_{ci}/E_{c1}$ is the plasticity number, E_{ci} is the initial modulus of elasticity of concrete and E_{c1} is the secant modulus obtained by connecting the diagram origin to the curve peak, i.e. (ε_{c1}, f_{cm}). The $E_c - \varepsilon_c$ relationship can be obtained from Eq. (2) taking into account that $E_c = \sigma_c/\varepsilon_c$ and $E_{c1} = f_{cm}/\varepsilon_{c1}$

$$E_c = -\frac{k-\eta}{1+(k-2)\cdot\eta}\cdot E_{c1} \quad \text{for} \quad \varepsilon_c < \varepsilon_{c,lim} \tag{3}$$

In Eq. (2), E_c is the secant modulus obtained by connecting the diagram origin to a point on the $\sigma_c - \varepsilon_c$ curve. The $\sigma_c - \varepsilon_c$ and $E_c - \varepsilon_c$ curves yielded by Eqs. (2) and (3) are schematically shown in Figure 4. It should be noted that the material formulation in the extended brittle cracking model does not explicitly include an increase of compressive strength in multiaxial compression. However, part of this effect takes place at the structural level when the confinement induced by the multiaxial compression prevents failure of concrete in tension in the direction perpendicular to the compressive load applied. This part was considered by the model. It was for example found that in the biaxial compression, the compressive load that the material can carry can increase by up to 25% depending on the ratio between compressive loads along each axis.

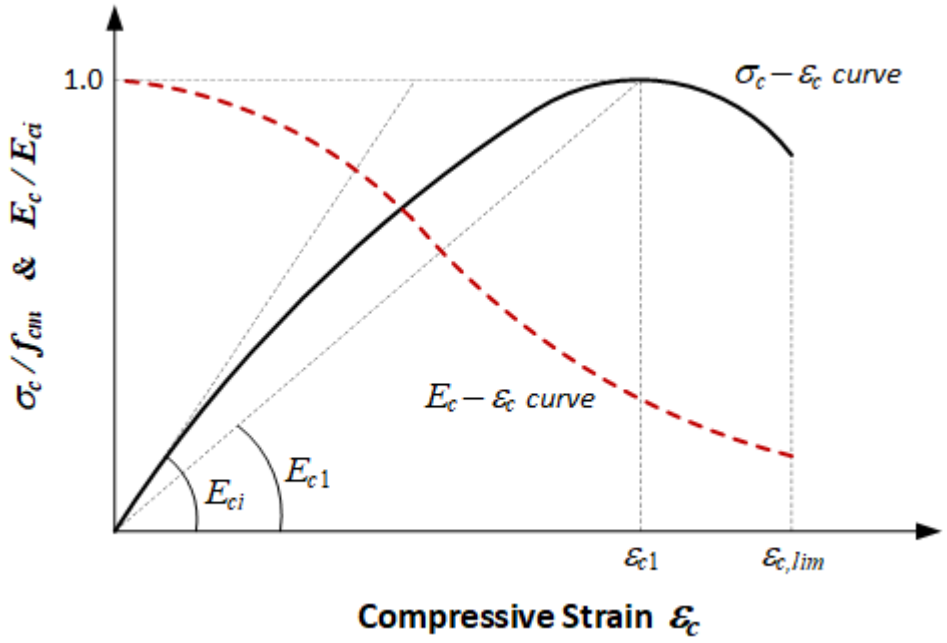

Figure 4. The $\sigma_c - \varepsilon_c$ and $E_c - \varepsilon_c$ curves describing Eqs. (2) and (3)

An additional advantage of the extended brittle cracking model is that it can be used together with an erosion algorithm that removes failed elements from the NLFEM model. The failure criterion is defined in this algorithm as the maximum compressive/tensile strain. The model has been validated by examining strain rate effects and simulating a number of benchmark cases including a three point bending test, a standard brittle failure test and a RC column under axial and blast loads [29, 50].

3.2. Validation at material level

Although it has been well established experimentally and numerically that the behaviour of plain concrete specimens (with a low moisture content) exhibits significant departures from that established during static loading once certain thresholds of applied loading rates (approximately 10 s^{-1} and 100 s^{-1} for uniaxial tension and compression, respectively, see Figure 5 and Figure 6) are surpassed [51, 52], there has been debate concerning the reasons that trigger this shift. All researchers agree that inertia has a significant effect on the behaviour exhibited by plain concrete specimens under high-rate loading; however, considerable disagreement exists regarding the influence of strain-rate sensitivity on the material properties of structural concrete. Many researchers consider that the material properties of concrete are

dependent on the rate of deformation (strain-rate dependency), e.g. [53, 54], a view which until recently was widely accepted and incorporated into the framework of existing military codes, e.g. [55], for the design and analysis of RC structures under blast and impact. Lately however, an increasing number of researchers [51, 52] have expressed the opposite view, stating that the material properties of structural concrete (characterised by a low moisture content) are essentially strain-rate independent and that the observed change in specimen behaviour with increasing loading rates is the result of (a) parameters affecting structural response, (b) the brittle nature and triaxiality characterising concrete material behaviour and (c) the nature of the problem at hand (a wave propagation problem within a highly nonlinear material).

The extended brittle cracking model was applied in this study for simulating an RC column subjected to a blast load. This material model does not explicitly account for the effect of high rate loading (strain-rate sensitivity) on the material properties of concrete. Therefore, it is important to establish the ability of the extended brittle cracking model to realistically describe a stress wave propagation problem within a highly nonlinear material medium such as concrete. To achieve this, the behaviour a concrete prism subjected to uniaxial tension or compression loads with increasing loading rates was investigated. The prism had a height of 253 mm and a 100 mm × 100 mm cross-section [51, 52]. Each edge of the prism cross-section was discretised into 5 elements, while the prism was divided into 13 elements along its height. This gave 125 elements with the dimensions of 20 mm $\times$ 20 mm $\times$ 19.5 mm. The concrete was modelled using 8-node linear brick elements (C3D8R) with reduced integration to prevent over-stiff elements and enhanced hourglass control to avoid spurious deformation modes in the model mesh [28]. The elements were controlled during the analysis to prevent excessive distortion of the mesh. The uniaxial compressive strength of concrete was assumed to be f_{cm} = 30 MPa, the modulus of elasticity equal to E_{ci} = 20 GPa, Poisson's ratio to ν = 0.2 and the density to ρ = 2400 kg/m^3. The stress-strain relationship describing the

behaviour of concrete in compression and the stress-displacement relationship describing the behaviour of concrete in tension were calculated using FIB Model Code [49], see Section 3.1.

The bottom face of the prism was fixed, and a uniform axial load was applied to the top face at different rates. To explain the response of the concrete prism to a high rate load, the dynamic problem must be viewed as a wave-propagation problem. The external load generated a uniform stress wave at the upper surface of the specimen. The stress wave propagated towards the lower part of the specimen. Because the specimen is fixed at the bottom, the stress wave rebounded off its bottom surface and moves back upwards. Once the stress wave reached the top specimen surface, it bounced back down again. The wave is therefore trapped by the specimen boundary conditions and continues moving up and down in the specimen. If energy dissipation mechanisms such as dumping, damage or adiabatic effects were incorporated in the model, the stress wave amplitude would gradually decrease.

The exhibited strain rate can be characterised in 3 ways, using (i) the average strain rate, (ii) the maximum value of the average strain rate and (iii) the applied stress rate. The average strain rate is calculated as the ratio between the displacement increment at the specimen top face divided by the length of the whole specimen. The maximum value of average strain rate is found by dividing the specimen into zones along the axis of symmetry and by evaluating which one of these zones exhibits the largest average strain rate. This type of strain rate characterisation is particularly relevant when carrying out Split Hopkins Pressure Bar tests [51]. The applied stress rate is defined as the load increment applied in each time step divided by the cross-sectional area of the specimen and the length of the time step used.

The effect of the loading rate under uniaxial tension was examined first. The load was applied in the form of displacement increments to stabilise the numerical solution during concrete failure in tension. Six different displacement rates ranging between 10 mm/sec and 20,000 mm/sec (corresponding to the maximum values of average strain rates between 0.0005 sec^{-1} and 3 sec^{-1}, respectively) were considered.

The value of the applied peak tensile stress increased with the growing levels of strain rate. Figure 5 shows the analysis results plotted together with the existing experimental data [51]. Note that the abscissa of the diagram in the figure is in a logarithmic scale, and the ordinate is the maximum dynamic reaction force, $R_{m,d}$, at the top face of the prism normalised by the maximum static reaction force, $R_{m,s}$. As can be seen, the numerical results fall within the experimental scatter, and the $R_{m,d}/R_{m,s}$ ratio increases more rapidly for the strain rates larger than 0.1 sec^{-1}. It is also necessary to note that the displacement loads with the rates larger than 20,000 mm/sec (i.e. the maximum value of average strain rate of 3 sec^{-1}) caused distortion of the finite elements, rendering the results unreliable.

The effect of the loading rate under uniaxial compression was examined next. The load was applied in the form of a pressure load. The load was increased monotonically to failure at rates ranging between 10,000 MPa/sec and 4,000,000 MPa/sec (corresponding to the maximum values of average strain rate between 0.01 sec^{-1} and 70.8 sec^{-1}, respectively). Figure 6 shows the results of numerical simulations as well as the existing experimental data [52]. Note that the abscissa of the diagram in the figure is in a logarithmic scale, and the ordinate is the maximum dynamic pressure, $P_{m,d}$, normalised by the maximum static pressure, $P_{m,s}$. It is evident that the growing strain rate leads to the increase of the $P_{m,d}/P_{m,s}$ ratio and this increase becomes more rapid for the strain rates larger than 0.3 sec^{-1}. In addition, the numerical results fall within the experimental scatter.

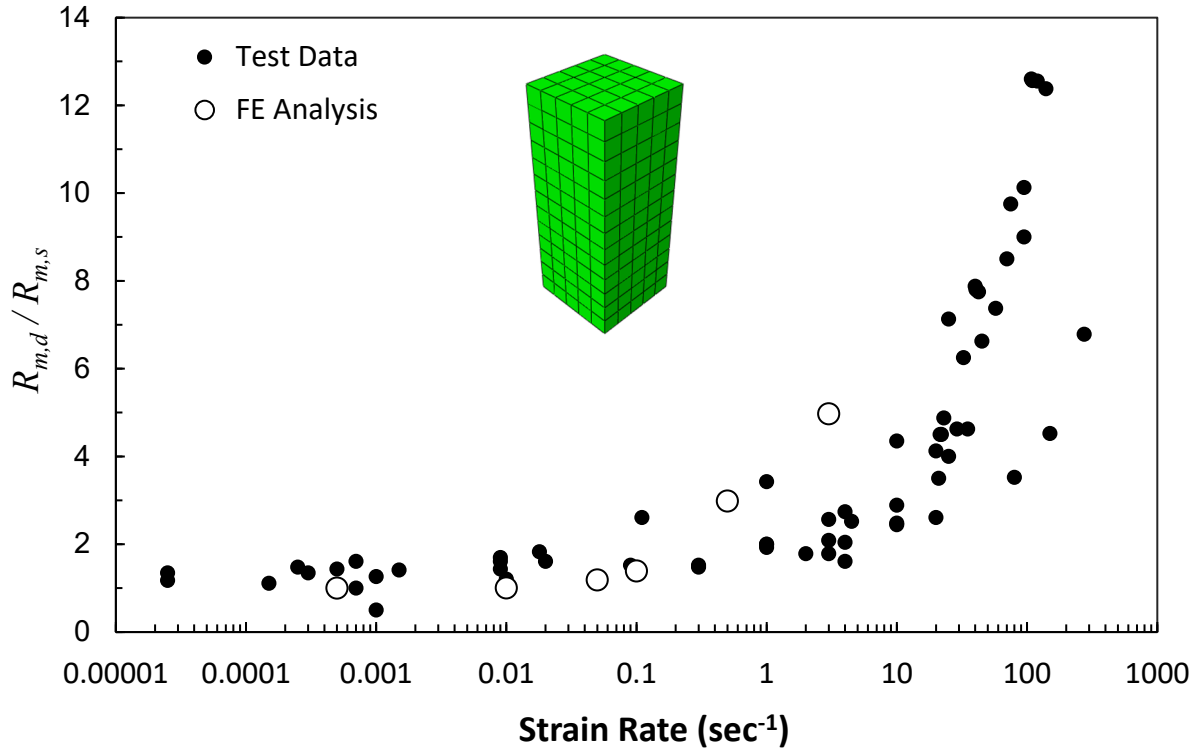

Figure 5. Effect of strain rate on the behaviour of concrete prisms subjected to uniaxial tension. The experimental data is taken from [51].

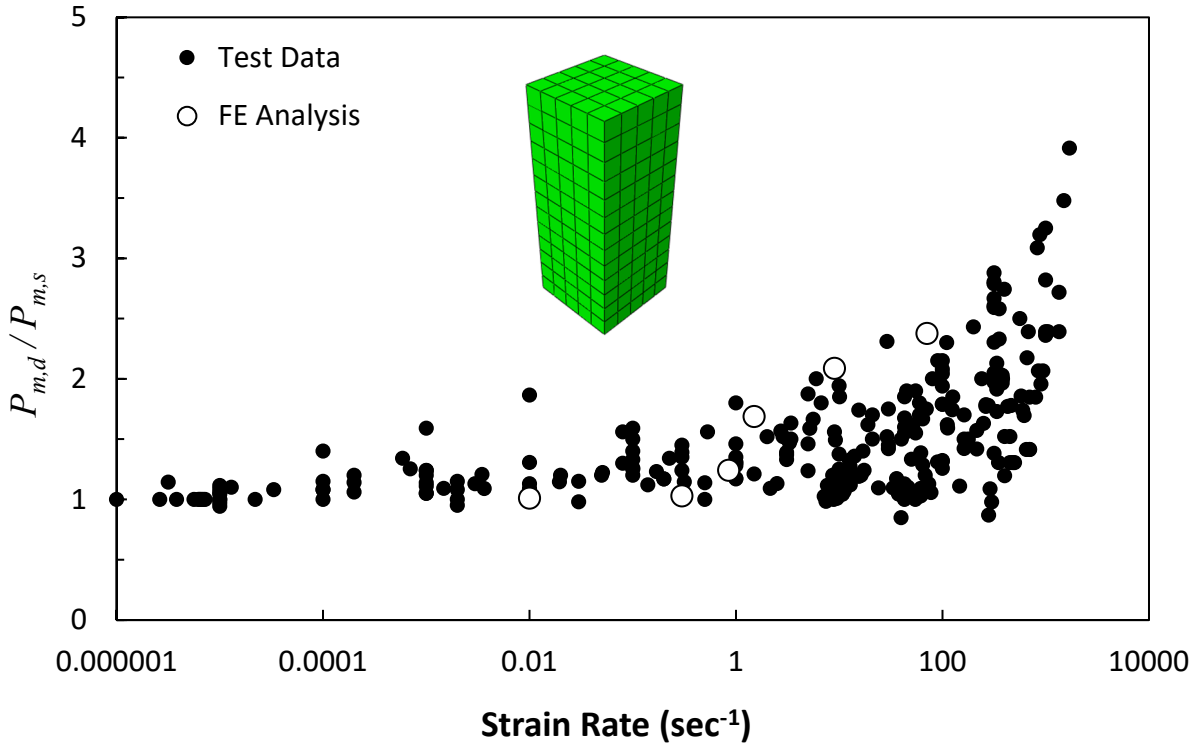

Figure 6. Effect of strain rate on the behaviour of concrete prisms subjected to uniaxial compression. The experimental data is taken from [52].

The constitutive material model introduced in this paper to describe the behaviour of concrete is based on the static, strain rate independent properties of the material. The comparative study between the numerical and experimental data revealed that the extended brittle cracking model is capable of providing realistic predictions of the behaviour of concrete at high rates of loading. In view of this, it can be concluded that the effect of the loading rate on the specimen's behaviour reflects the positive effect of the inertia loads on the specimen strength.

The development of compressive and tensile strain rates in the RC column used in this study for derivation of pressure-impulse diagrams (see Section 3.4 for details) was investigated to evaluate the ranges of maximum strain rates. The analyses of the column response to several cases of impulsive, dynamic and quasi-static loads (achieved with different combinations of peak pressure and impulse) showed that the largest compressive and tensile strain rates developed in the column at supports, where maximum damage occurred. The maximum values of both the compressive and tensile strain rates in the concrete reached only up to 2 s^{-1} after which the concrete elements failed by cracking in tension or crushing in compression and were removed from the model using the erosion algorithm in Abaqus. It should be noted that in most cases the strain rates were much lower than 2 s^{-1}. The maximum strain rates occurred for short periods of only a few tenths of a microsecond and in a highly localised volume of concrete. Comparing the values of strain rates predicted from the NLFEM analyses with the thresholds (i.e. approximately 10 s^{-1} for uniaxial tension and 100 s^{-1} for uniaxial compression, see Figure 5 and Figure 6) shows that the strain rate effect is unlikely to result in an increase of concrete strength that could, in turn, affect structural behaviour.

3.3. Validation at structural level

An accurate derivation of P-I diagrams depends on understanding the mechanics underlying RC structural response under a range of loading regimes. The validation of the extended brittle cracking model at the structural level was performed at the quantitative and qualitative levels using the computational

simulation of tests on RC columns from [56] and [57]. The first RC column simulated was a ground floor central column in a two-story, quarter-scale framed RC structure subjected to a blast load (test No. 2 in [56]). The RC column had 85 mm × 85 mm cross section and 900 mm height. It was reinforced by 8 longitudinal bars with 3.2 mm diameter and 1.6 mm diameter hoops spaced at 100 centres. The cover depth was 8.5 mm. The unconfined concrete strength was equal to f_{cm} = 42 MPa and the modulus of elasticity equal to E_{ci} = 24 GPa. The yield and ultimate stresses of longitudinal steel were equal to 450 MPa and 510 MPa, respectively. The yield and ultimate stresses of hoops were equal to 400 MPa and 610 MPa, respectively. The modulus of elasticity of steel was 210 GPa, and the fracture strain was 18%.

The explosion was generated by 7.1 kg of C-4 located at a standoff distance of 1.07 m, which was the distance from the centre of charge to the column face. The study [56] reports pressure-time and impulse-time histories for two points on the column front face at about 34% and 0.85% of the column clear height. These time histories were complex and differed from each other. Additionally, the peak pressure occurred at different times at these two points and different peak pressure values indicated a non-uniform distribution of pressure over the column height. The quarter scale-column from test No. 2 in [56] has been used for validation of numerical models in several research works, e.g. [1, 6, 58]. In these works, the blast load was described as an equivalent pressure load with a triangular load-time history with zero-rise time applied uniformly over the column front face. The average equivalent peak pressure was taken as 7 MPa and the impulse as 1.1 MP·msec, which resulted in the duration of the simulated blast load equal to 0.314 msec. In this study, a similar method was adopted for the validation of the numerical model.

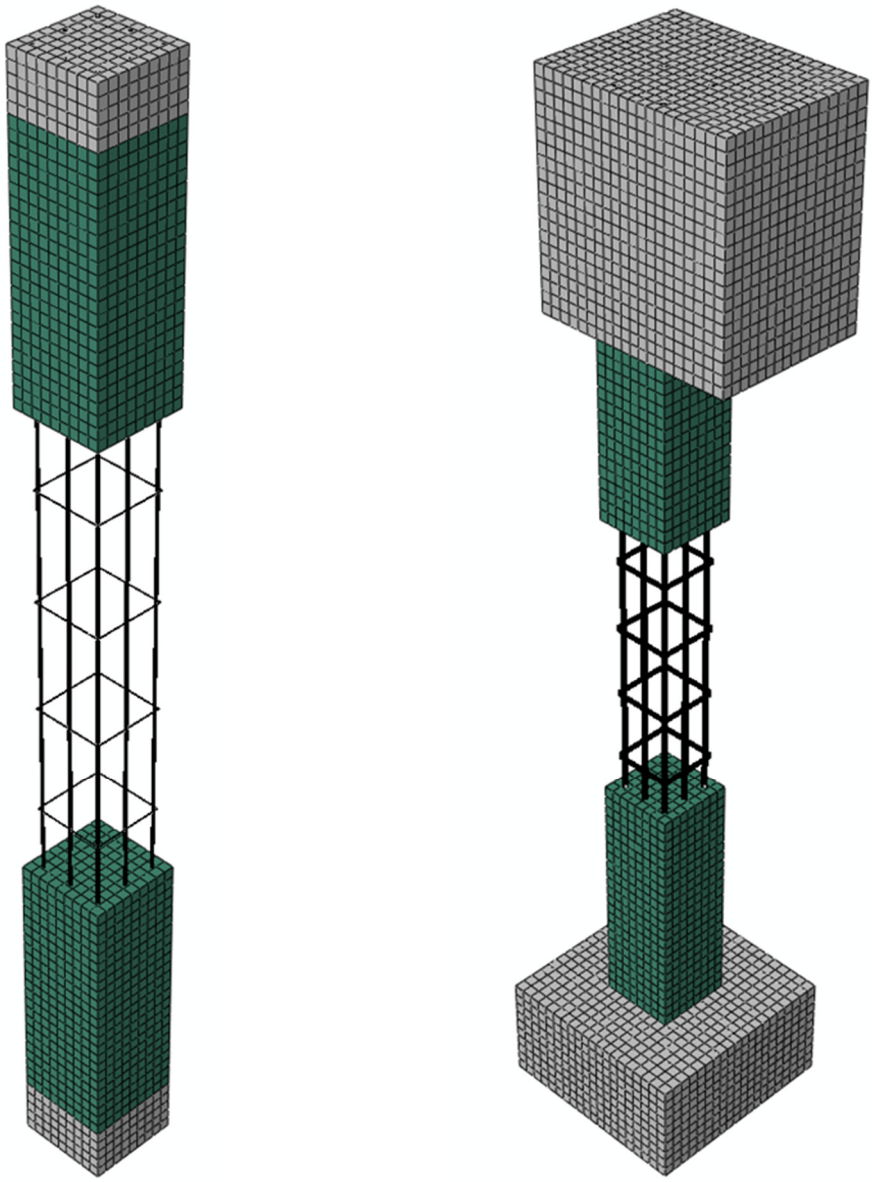

(a) (b)

Figure 7. NLFEM models of RC columns from (a) [56] and (b) [57].

The concrete material was modelled using the extended brittle cracking model, where FIB Model Code [49] was used for calculation of parameters. The modelled column was connected monolithically to a RC slab and a RC foundation at the ends. To consider the effect of boundary conditions on column behaviour, heading and footing were added to the model. Both the heading and footing had the column cross-section, 50 mm height and were modelled as linearly elastic with the modulus of elasticity of concrete. The

longitudinal reinforcement extended to the heading and footing. To simulate boundary conditions within a framed structure with floor slabs, all nodes on the back and side vertical faces (facing away from and across to the explosion source) of the heading and footing were restrained in the horizontal plane, while the top and bottom faces of the footing was restrained in vertically. The concrete was modelled using the same 8-node linear brick elements (C3D8R) as in the prism described in Section 3.2. A mesh sensitivity analysis was performed, and the mesh size of 1mm was selected for the model. Reinforcing bars were modelled using Timoshenko beam elements (B31) and classic metal plasticity [28]. The use of the beam elements for modelling reinforcement enabled to include the effect of the dowel action of steel bars in the column model. The reinforcing bar elements were embedded in the concrete elements. This formulation assumed perfect, unfailing bond between steel bars and concrete. The NLFEM column model with exposed reinforcement is shown in Figure 7a.

As was discussed in Section 3.2, the development of tensile strain rates in an RC column subjected to impulsive, dynamic and quasi-static loads was investigated. The maximum values of the tensile strain rate in reinforcing bars reached in only a few cases to about 0.3 s^{-1}, while in most cases they were much smaller. The strain rate of 0.3 s^{-1} could result in yielding strength amplification of up to about 1.5 [59]. The development of high strain rates occurred in the reinforcement for very limited periods of a few tenths of a microsecond over a very limited bar length (a few centimetres) in only a few places. It should also be noted that the ultimate strength is less sensitive to strain rate and the strength amplification effect becomes significant only for strain rate values larger than 1 s^{-1}. Therefore, considering the strain rate sensitivity in the numerical analysis was expected to have an insignificant effect on structural response, which justifies the use of the static material properties for describing the steel material behaviour in the present investigation.

The measured and calculated displacement time histories at the middle of the column are plotted in Figure 8. The comparison between the experimental and calculated results shows that the NLFEM column was

slightly stiffer and developed about an 8% lower peak displacement which occurred about 19% earlier than the measured one. The residual displacement recorded in the tests was 6.5 mm which is about 3% larger than the calculated one.

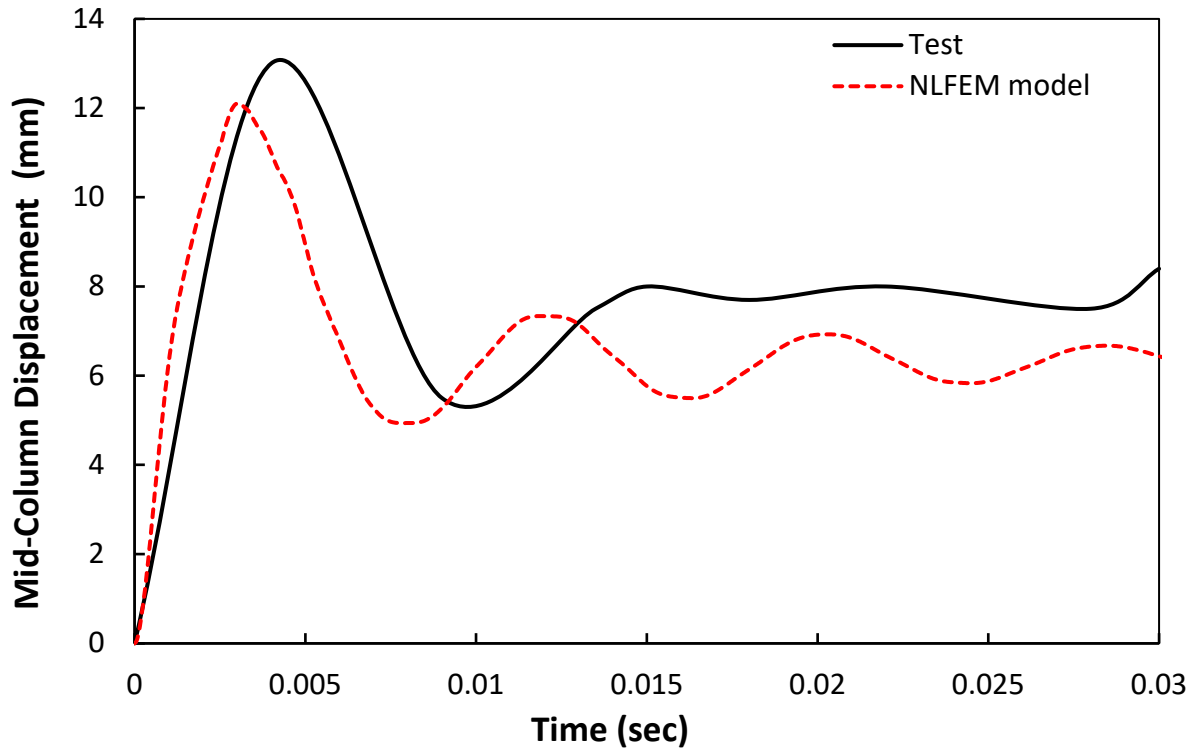

Figure 8. Time history of mid-column displacement obtained in tests [56] and NLFEM model.

An additional validation of the extended brittle cracking model at the structural level was performed using the results of tests on two RC columns, conducted by the Explosive Loading Laboratory [57]. This laboratory was designed to simulate the impulse delivered by an actual blast to a structure and to be able to measure the structural response in a controlled environment. The simulated blast loads were produced by an array of four blast generators, which were made up of an impacting module and a hydraulic actuator. The tested columns were casted with heavily reinforced heading and footing. The footing was connected to the test floor by four bolts and restrained in the direction of the applied load by an RC block. The heading was restrained from horizontal movements, and horizontal and in-column-plane rotations by a link system. The vertical movement of the heading was not restrained allowing for the application of axial load by

means of three hydraulic jacks attached to a vertical load frame. This setup enabled the simulation of initial gravity load on the column.

In this work, Test 7 and Test 8 columns were considered. Both columns were 3277 mm high (excluding heading and footing) with a 356 mm × 356 mm cross-section and were reinforced with eight #8 longitudinal reinforcing bars and #3 hoops at 324 mm centres. The cover to the hoops was 38 mm. The concrete had compressive strength of f_{cm} = 40 MPa and the modulus of elasticity of E_{ci} = 24 GPa. The modulus of elasticity of steel was equal to 210 MPa, the yield strength of the longitudinal bars to 335 MPa and of the hoops to 235 MPa. The columns were subjected to simulated blast loads, the time histories of which are shown in Figure 9. The Test 8 column was additionally loaded by three hydraulic jacks with a static axial force of 445 kN prior to the application of the blast load. The validation of the extended brittle cracking model against Test 8 is especially valuable, since an RC column with different axial loads will be used in the demonstration of the extended P-I diagram method in Sections 4 and 5.

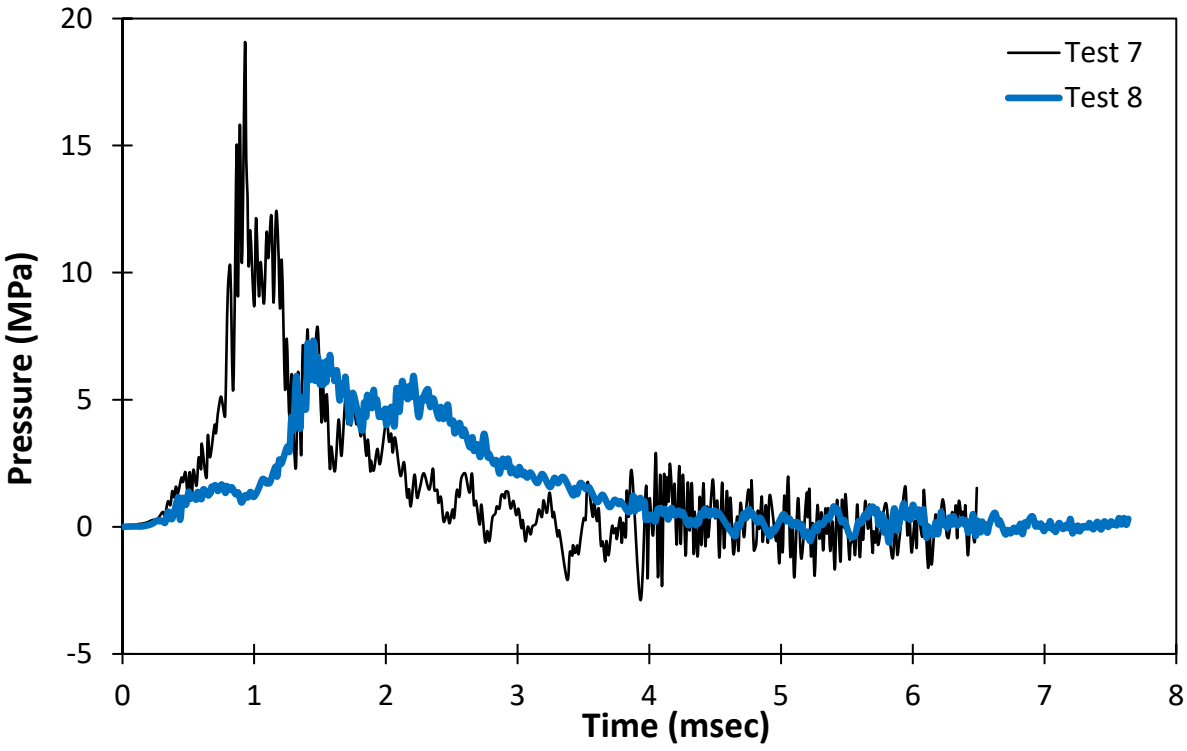

Figure 9. Simulated blast load time histories of Test 7 and 8, taken from Figures 3.44 and 3.58 in [57].

The NLFEM model of the column from the Tests 7 and 8 included both the heading and footing, as shown in Figure 7b. Since the footing was fully restrained in the tests, its supporting condition was modelled by restraining each face of the footing in perpendicular direction. The restraint system of the heading allowed only the vertical displacement. This supporting condition was modelled by restraining the movement of the heading back face (away from the blast) in the horizontal plane. Since the footing and heading were confined and heavily reinforced, they were modelled as linearly elastic with the modulus of elasticity of concrete. The concrete column was modelled using 16224 solid elements. The reinforcing bars were modelled using 1372 Timoshenko beam elements (B31) and were embedded in the concrete elements. The blast load was simulated by applying a uniform pressure load over the front (blast-facing) column face. The axial load was applied on the Test 8 column gradually to avoid any inertial effects as a uniform pressure distributed over a column-wide strip located on the top of the heading directly above the column.

In the test, the Test 7 column underwent shear failure by developing inclined bands of crushed concrete at both ends, spalling of concrete cover and deformation of reinforcing bars in the bands. The peak mid-height deflection of 122 mm was developed at 41.7 msec from the beginning of the test. Figure 10 shows three stages of the numerical simulation of Test 7. As can be seen, the column failed in shear at the footing and heading. The shear failure started at about 2 msec after the application of the blast load by the development of inclined cracks (see Figure 10a). The shear cracks grew and interconnected into inclined bands. The concrete in these bands is severely damaged by the end of the blast load, i.e. by 7 msec after the blast load application (see Figure 10b). The conditions of the column at the time of the peak mid-span defection (i.e. 36.9 msec) is shown in Figure 10c. As can be observed, the disintegration of concrete in the inclined shear bands continued.

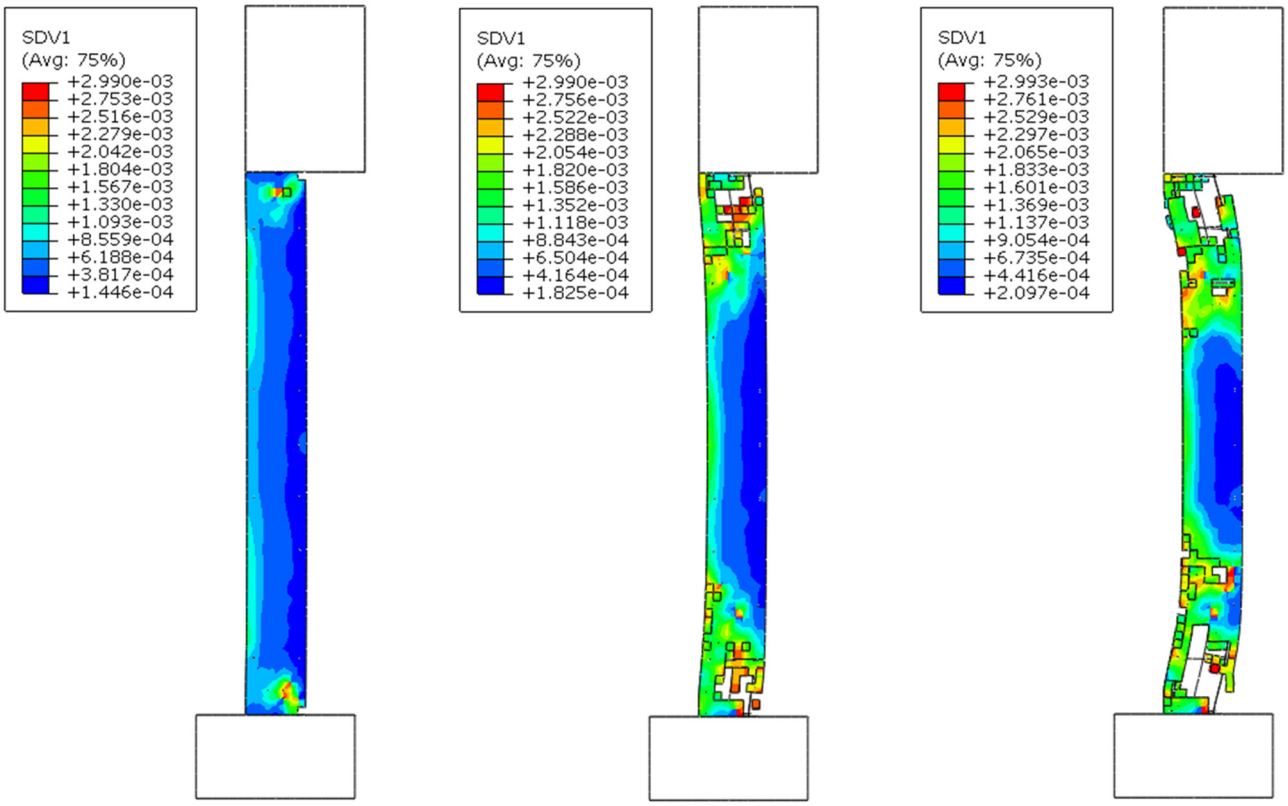

(a) (b) (c)

Figure 10. NLFEM simulations of the Test 7 column at the time of (a) 2 msec, (b) 7 msec and (c) 36.9 msec (the time of the peak mid-height deflection) after blast load application. SDV1 in the legend stands for the absolute value of compression strain.

The post-loading conditions of the Test 7 column are shown in Figure 11a for 200 msec after the application of the blast load. The NLFEM model developed similar damage, which consisted of inclined bands of crushed concrete at column ends. The peak deflections recorded at 36.9 msec of the NLFEM simulation was equal to 114.3 mm, which underestimated the experimental deflection by 6.3%. The bands of crushed concrete developed at column ends in the NLFEM model and the test are compared in Figure 11a. The approximate boundaries of the bands developed in the tests are shown as dashed lines. As can be seen, there is good qualitative agreement between the column responses in both cases. Although, the top band in the test is slightly narrower.

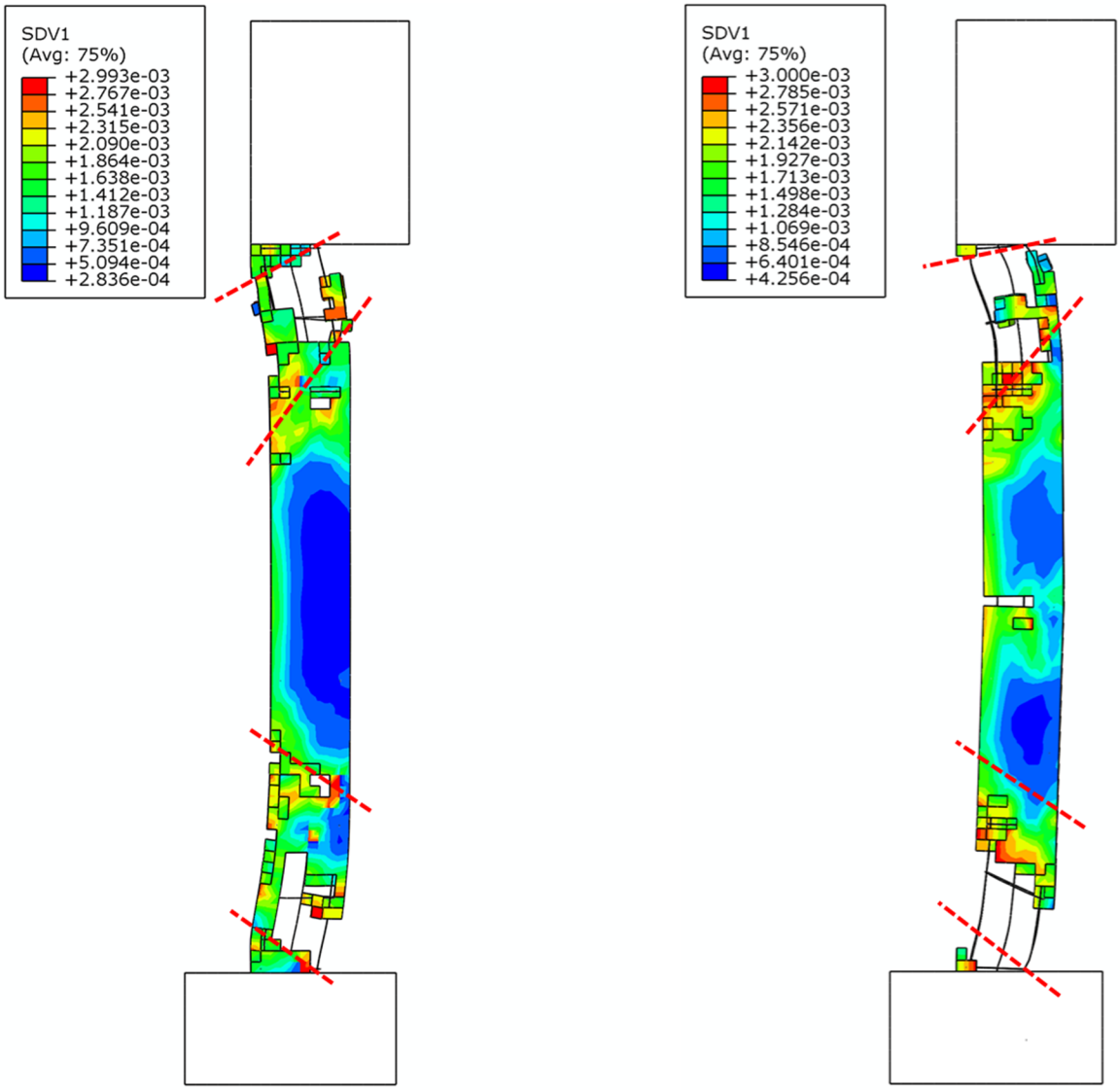

(a) (b)

Figure 11. NLFEM simulations of (a) Test 7 and (b) Test 8 columns at 200 msec after blast load application. Dashed lines indicate the approximate locations of failure zones obtained in tests [57]. SDV1 in the legend stands for the absolute value of compression strain.

The development of damage in the Test 8 column obtained from the numerical simulation is shown in Figure 12. The first signs of damage appeared at about 2 msec from the blast load application as horizontal shear cracks on the back face of the column at the footing and heading (see Figure 12a). These cracks grew and interconnected with inclined shear cracks into inclines shear bands visible by the end of the blast load, i.e. by 7 msec after the blast load application (see Figure 12b). Additionally, a zone of crushed concrete developed at the column mid-height and started to grow horizontally from the loaded face into the column

depth. At the time of the peak mid-height deflection shown in Figure 12c, the column sustained heavy damage in the shear bands, where large regions of concrete disintegrated exposing the reinforcement.

The failure mechanism of the Test 8 column was, in general, similar to the Test 7 column. Both columns developed two inclined shear bands with crushed concrete at the heading and footing (see Figure 11). However, the presence of the axial load resulted in larger damage (larger regions of disintegrated concrete) in the Test 8 column. The maximum mid-height horizontal deflection of 157 mm was recorded in the Test 8 column at 47.6 msec. The maximum downward deflection of the Test 8 column heading was 36.8 mm at 53.3 msec. This downward deflection caused extension of the hydraulic jacks which should have resulted in the decrease (and possibly elimination) of the axial load. To account for this effect, the axial load in the NLFEM model was gradually reduced to zero after the application of the blast load. The post-loading condition of the Test 8 column is shown in Figure 11b for 200 msec after the blast load application. The scenario of the NLFEM column failure corresponded to its physical counterpart. Inclined bands of crushed concrete developed, the concrete cover spalled and reinforcing bars deformed in both the test column and numerical model. The peak mid-height deflection of 143.5 mm occurred at 49 msec from the beginning of the simulation. The peak deflection was underestimated by 8.6%. The maximum downward deflection of the heading was equal to 44.5 mm, which developed at 54.9 msec from the application of the blast load. The maximum axial deflection was overestimated by 20.9%. In Figure 11b, the included bands of the crushed concrete developed in Test 8 are indicated with dashed lines. The comparison between the tests and numerical model shows that the bottom band in the model is narrower than in the tests, while the top band in the model is wider than in the test. Additionally, the zone of crushed concrete in the middle of the column model reached through more than half of the column depth. This behaviour was not observed in the test.

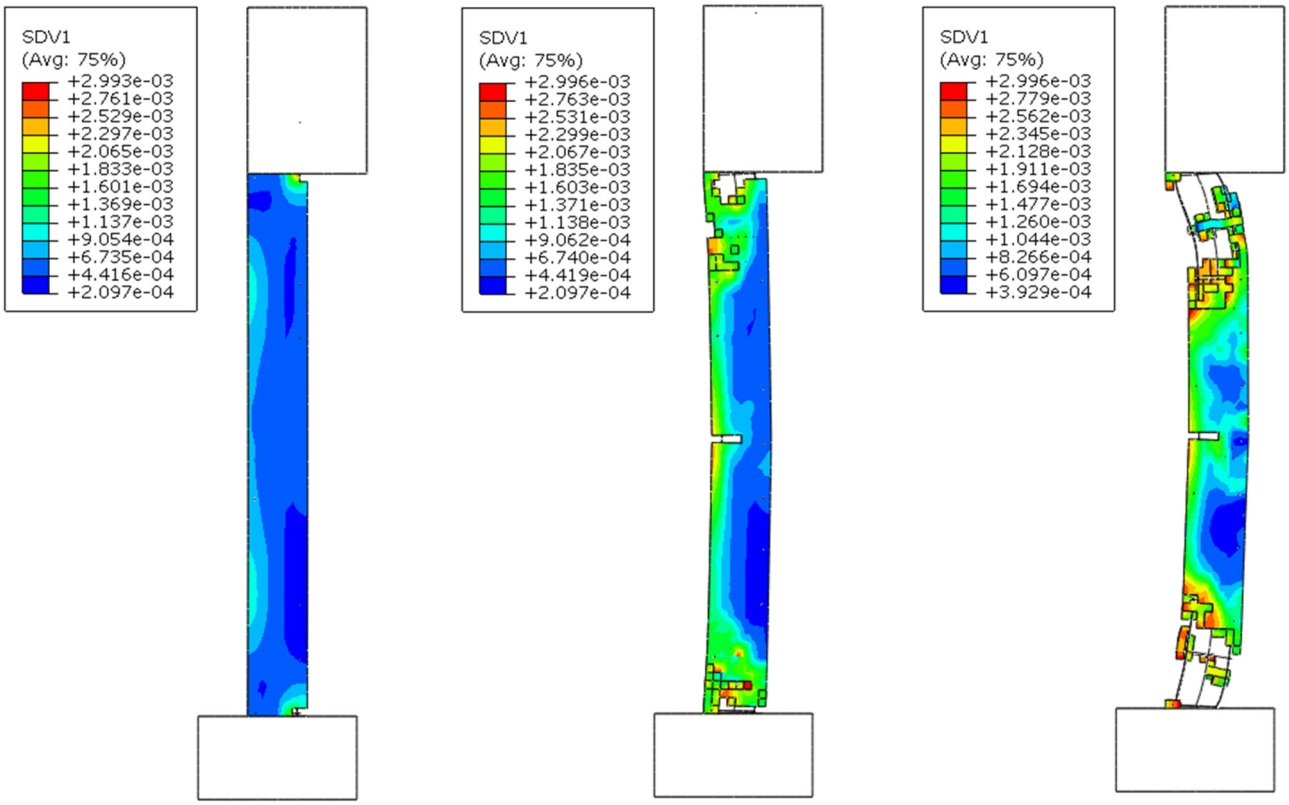

(a) (b) (c)

Figure 12. NLFEM simulations of the Test 8 column at the time of (a) 2 msec, (b) 7 msec and (c) 49 msec (the time of the peak mid-height deflection) after blast load application. SDV1 in the legend stands for the absolute value of compression strain.

The differences between the tests and the numerical simulations shown in Figure 11 can be explained by the effects of several approximations included in the NLFEM models. The blast loads were applied in the tests through an array of four blast generators, while in the simulations, the blast loads were modelled as uniformly distributed equivalent pressure with the time history reported in [57]. The boundary condition of the heading in the Test 8 column allowed for some rotation due to the final stiffness of the links system, while the rotation of the heading was entirely prevented in the model. The changes of the axial force during the simulations of Test 8 were approximately modelled due to the luck of data. The contact between the reinforcing bars and the concrete elements was not defined in the NLFEM models. This led to the loss of confinement provided by the reinforcing bars to the concrete after the removal of the concrete elements in which the bars were embedded.

The development of P-I diagrams also requires accurate prediction of the behaviour of structures under static loads. To examine the performance of the extended brittle cracking model under static loads, the Test 7 column is gradually loaded by pressure uniformly distributed over the front column face. Initially, the column exhibits an elastic flexural behaviour up to the pressure p = 0.09 MPa. Since the width of the loaded front face is a = 356 mm, the column is loaded by a uniformly distributed load of $w = pa$ (per column length). The maximum moment at the supports (footing and heading) of the column is $M = wh/12$, where h is the column height. The elastic section modulus of a square cross-section is $Z = a^3/6$. The maximum elastic stress in the column $\sigma_{max} = M/Z$ reaches the concrete tension strength of 3.6 MPa at p = 0.09 MPa and first cracks develop at the column ends. It was observed that the stresses concentration at the column-footing connection were higher than at the column-heading connection. This was the result of a higher rotational confinement produced by the footing due to a different geometrical configuration. Therefore, the first flexural horizontal crack initiated on the loaded column face at the column-footing connection. A second flexural horizontal crack initiated at the column-heading connection. The cracking process proceeded by the development of additional horizontal cracks located further from the footing and heading. Additional flexural cracks started to develop at the column mid-height (i.e. in the secondary zone of maximum moments) at the pressure of p = 0.19 MPa. Figure 13a shows the distribution of the maximum principal strain in the column at the pressure of p = 0.5 MPa. The strain concentrations at the supports and mid-height of the column correspond to the flexural cracks. As can be seen, three horizontal cracks developed at the footing and only two cracks at the heading due to the differences in the boundary conditions. At this point, the longitudinal reinforcement in the cracked zones at the heading and footing developed a tensile stress of 300 MPa, while the tensile stress in the hoops is very low, reaching only 41 MPa. This tensile stress distribution in the reinforcement supports the purely flexural response of the column. The column exhibited flexural response up to the pressure of p = 0.55 MPa, after which the shear response dominated the column behaviour. At this pressure loading, first shear cracks

developed. The longitudinal bars in the cracked zones at the heading and footing yielded. The tensile stress in the hoops reached 233 MPa, which is just under the hoop yielding stress of 235 MPa. Figure 13b shows the development of first shear cracks at the footing and heading of the column subjected to the pressure of 0.6 MPa. Note that the shear cracks connected the tips of the flexural cracks. At this pressure, first hoops in the zones with shear cracks yielded. The tensile stress gradually increased in the longitudinal bars in the tensile zone at the column mid-height, which indicated the development of plastic hinges at the heading and footing. Additional shear cracks developed with increasing load and interconnected into two inclined bands, where the concrete crushed and disintegrated and more hoops yielded (see Figure 13c showing the column subjected to the pressure of 0.8 MPa).

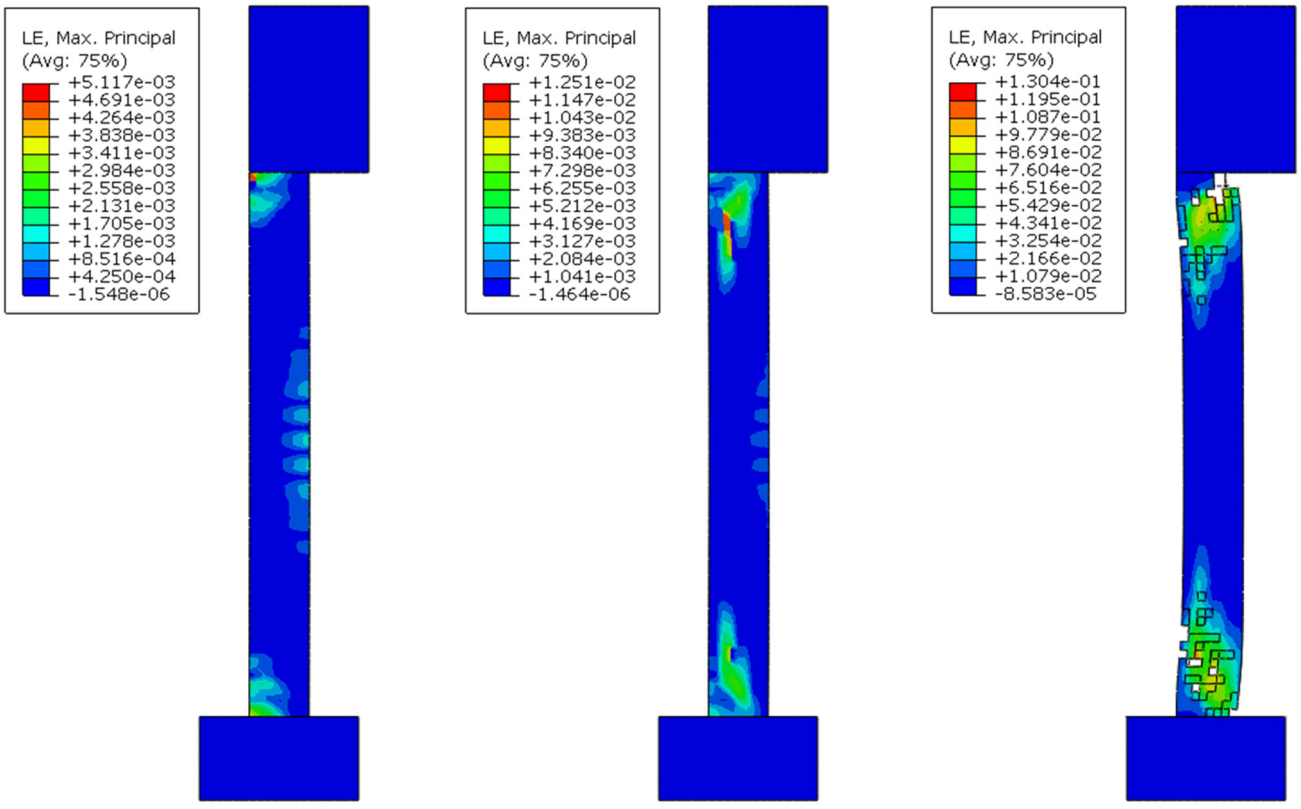

(a) (b) (c)

Figure 13. FE simulations of the Test 7 column loaded statically by uniform pressure over the front column face: (a) pressure of 0.5 MPa, (b) pressure of 0.6 MPa and (c) pressure of 0.8 MPa. LE in the legends stands for the maximum principal strain.

It can be finally concluded based on the four validation cases performed that the developed NLFEM model can provide reliable predictions of the behaviour of RC columns in different loading regimes.

3.4. RC column model

A full-scale RC column applied in Sections 4 and 5 for the demonstration of the extended P-I diagram method is 3 m high and has a 300 mm × 300 mm cross-section and 30 mm cover to reinforcement. The reinforcement consists of eight 18 mm diameter longitudinal bars and 10 mm diameter hoops spaced at 200 mm centres. The column has 200 mm high heading and footing to simulate boundary conditions within a framed structure. Both the heading and footing have a 300 mm × 300 mm cross-section and are modelled as linearly elastic with the modulus of elasticity of concrete. All nodes on the back vertical faces (facing away from the blast) of the heading and footing were restrained in the horizontal plane, while the bottom face of the footing was restrained in vertically. The top face of the heading was used for the application of the axial load.

The concrete material was modelled using the extended brittle cracking model with the modulus of elasticity equal to E_{ci} = 24 GPa and the unconfined concrete strength to f_{cm} = 40 MPa. FIB Model Code [49] was used for the calculation of the parameters of the extended brittle crack model. The concrete and reinforcement were modelled similarly to the quarter-scale column in Section 3.3. A refined mesh of 50 mm was used in all FE simulations based on the element size sensitivity analysis [29, 50]. The modulus of elasticity of reinforcing steel was equal to 210 GPa, the yield stress of longitudinal bars to 335 MPa and of hoops to 235 MPa.

4. Derivation of diagrams

The extended P-I diagram method is demonstrated for the RC column described in Section 3. The column is subjected the axial and blast loads. The axial load (*N*) is used for derivation of complementary (*N*-*I* and *N*-*P*) diagrams. All diagrams are derived for 3 levels of damage (i.e. low, medium and high damage). Since

the main purpose of columns is to carry axial loads, the residual axial carrying capacity is considered as the failure criterion. It is necessary to note that this failure criterion is not entirely practical as it cannot be measured directly as, for example, the mid-height column deflection or support rotation. However, it is important for the practicing engineers to know the residual axial loading carrying capacity of the blast-damaged columns. To evaluate the residual axial capacity, each computational simulation was performed in three analysis steps shown in Figure 14. In Step 1, the column was loaded by the axial force. In Step 2, the blast load was applied. In Step 3, an additional axial force was introduced until the column collapsed. The time history of the loading steps and the flowchart describing main steps undertaken in each FE simulation are depicted in Figure 14.

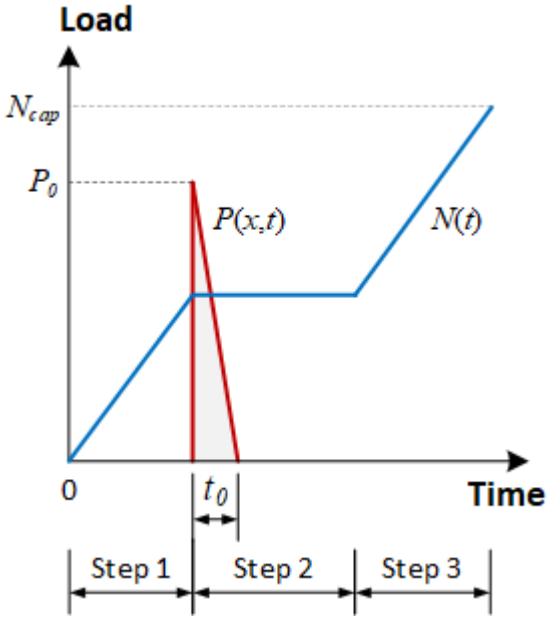

Figure 14. NLFEM analysis steps

In order to ensure static behaviour in Steps 1 and 3 the axial force was loaded in a gradual manner to avoid the development of inertia effects. In Step 1, the axial force was applied as an equivalent pressure on the top surface of the heading. In Step 2, the axial force remained constant. The blast load was simulated through application of uniform pressure on the front vertical face (facing the explosion source) of the column. The blast load had a triangular shaped time history with zero rise time. After the application of the blast load, Step 2 lasted sufficiently long to allow for dissipation of the blast-induced energy. In Step

3, the vertical degree of freedom of the top surface of the heading was confined. The pressure on the top surface was deleted and vertical displacement imposed. The axial force in the column was calculated form the vertical reactions. This setup assured stability of computational simulations. After the completion of Step 3 the structural damage, d, was found according to the following formula:

$$d = \left(1 - \frac{RF_{v,3}}{N_{cap}}\right) \times 100\% \quad (4)$$

where N_{cap} is the ultimate axial capacity of an undamaged column obtained in a separate analysis and $RF_{v,3}$ is the maximum vertical reaction force from Step 3. N_{cap} was found using NLFE analysis as equal to N_{cap} = 2570 kN. The P-I curves were derived for 20%, 50% and 80% damage that represented the borderlines between the low ($d < 20\%$), medium ($20\% < d < 50\%$) and high ($50\% < d < 80\%$) damage levels, e.g., see[1].

4.1. P-I diagrams

The derivation of P-I curves using the NLFEM analysis requires generation of multiple points on the P-I plane by multiple simulations of the column subjected to a blast load with different combinations of peak pressure P_0 and impulse I. To make the process of curve derivation more efficient, various search algorithms can be applied [7]. These search algorithms can be divided into a pressure-controlled, impulse-controlled or mixed unidirectional search. The pressure-controlled search is based on the gradual increase of the duration of the blast load t_0 (and hence its impulse) in each simulation, while maintaining P_0 constant. The duration t_0 is increased whilst the limit state condition $G \leq 1$ (see Eq. (1)) is satisfied. This search results in a horizontal series of points on the P-I plane for each P_0 (see sets PI3a and PI3b in Figure 15). The impulse-controlled search is based on the gradual increase of P_0 in each simulation till $G \geq 1$. In this case, t_0 is gradually decreased to keep I constant. This search algorithm results in a vertical series of points on the P-I plane generated for each I (see sets PI2a and PI2b in Figure 15). In the mixed search, both P_0 and I (and so t_0) gradually increase in accordance with a certain linear proportionality rule $P_0 = \alpha I$,

where α is a proportionality coefficient. This search algorithm results in a series of points along an inclined line emerging from the origin of the P-I coordinates (see sets PI1, NI1 and NP1 in Figure 15). The inclination angle of the line is governed by α.

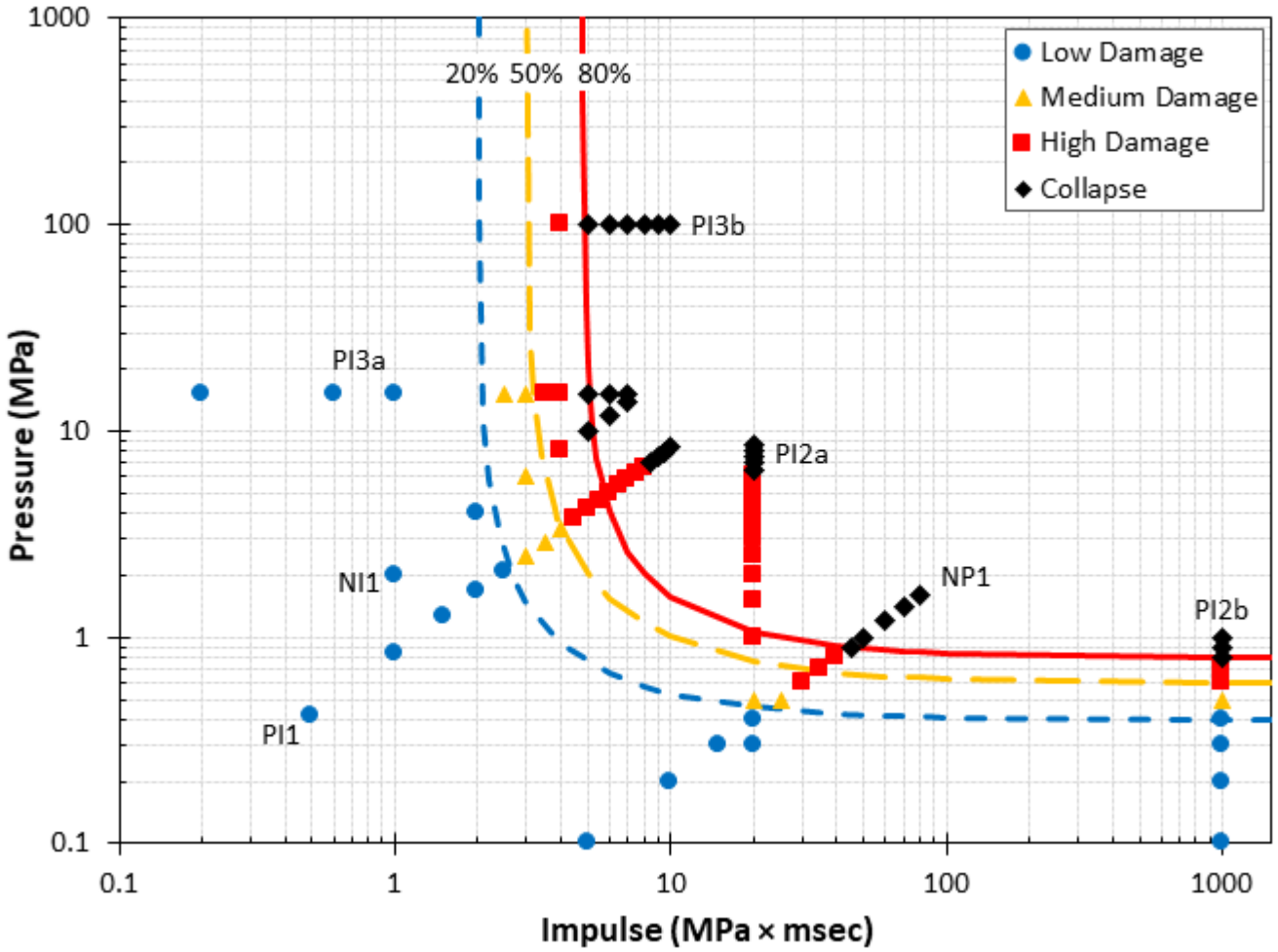

Figure 15. Data sets obtained using NLFEM analyses and P-I curves fitted for 20%, 50% and 80% damage levels. The axes are in logarithmic scale.

Three P-I curves, corresponding to the 20%, 50% and 80% damage, levels were initially derived for the axially unloaded RC column described in Section 3. An optimised procedure for diagram derivation was applied. First, the mixed search algorithm was used to establish the ranges for the three damage levels considered in the dynamic region and provide information on the pressure and impulse ranges in the impulsive and quasi-static regions. The application of this algorithm resulted in the three sets PI1, NI1 and NP1, as shown in Figure 15. Second, the impulse-controlled search algorithm was applied to establish the ranges for the three damage levels in the quasi-static region. Two sets PI2a and PI2b were generated

through the application of this algorithm, see Figure 15. Third, the pressure-controlled search algorithm was applied for establishing the three damage ranges in the impulsive region, which resulted in the sets PI3a and PI3b.

The PI data sets shown in Figure 15 were further used for derivation of three P-I curves representing 20%, 50% and 80% damage levels. A following expression was used for description of the P-I curves, e.g., see [33],

$$(P_0 - A_P)(I - A_I) = (C_P \cdot A_P + C_I \cdot A_I)^D \quad (5)$$

where C_P, C_I and D are the constants. Fitting of Eq. (5) to the P-I data sets resulted in the values of the constant C_P = 1, C_I = 1 and D = 0.5, while the asymptotes equal A_I(20%) = 2 MPa·msec, A_I(50%) = 3 MPa·msec, A_I(80%) = 4.8 MPa·msec, A_p(20%) = 0.4 MPa, A_p(50%) = 0.6 MPa and A_p(80%) = 0.8 MPa.

4.2. Axial Force-Impulse diagrams

Three axial Force-Impulse (N-I) diagrams, corresponding to the 20%, 50% and 80% damage levels, were derived using the mixed search algorithm. The axial force was fixed in one set of NLFEM simulations. The first data set (NI1) was obtained from the analyses of the axially unloaded column (i.e. N = 0 kN). The axial force was increased between simulation sets (NI2-4) by the increments of ΔN = 625 kN. In all simulations, the duration of the blast load was kept equal to t_0 = 1 msec to induce the impulsive loading regime. The increase in the impulse by ΔI = 1 MPa·msec was achieved by increasing the peak pressure by ΔP_0 = 2 MPa, which introduced a linear relationship between P_0 and I. Each data set represents a sequence of horizontal points in Figure 16. Note that the horizontal data set NI1 becomes inclined in Figure 15 due to the use of the mixed search algorithm.

Fitting the data sets in Figure 16 showed that the N-I curves are described well with the following dimensionless expression

$$\frac{N}{N_{cap}} + \left(\frac{I}{A_I}\right)^b = 1 \quad (6)$$

where the exponent b equals 1.5, 1.6 and 1.8 for the 20%, 50% and 80% damage, respectively. The three N-I curves derived for the low, medium and high damage levels are presented in Figure 16.

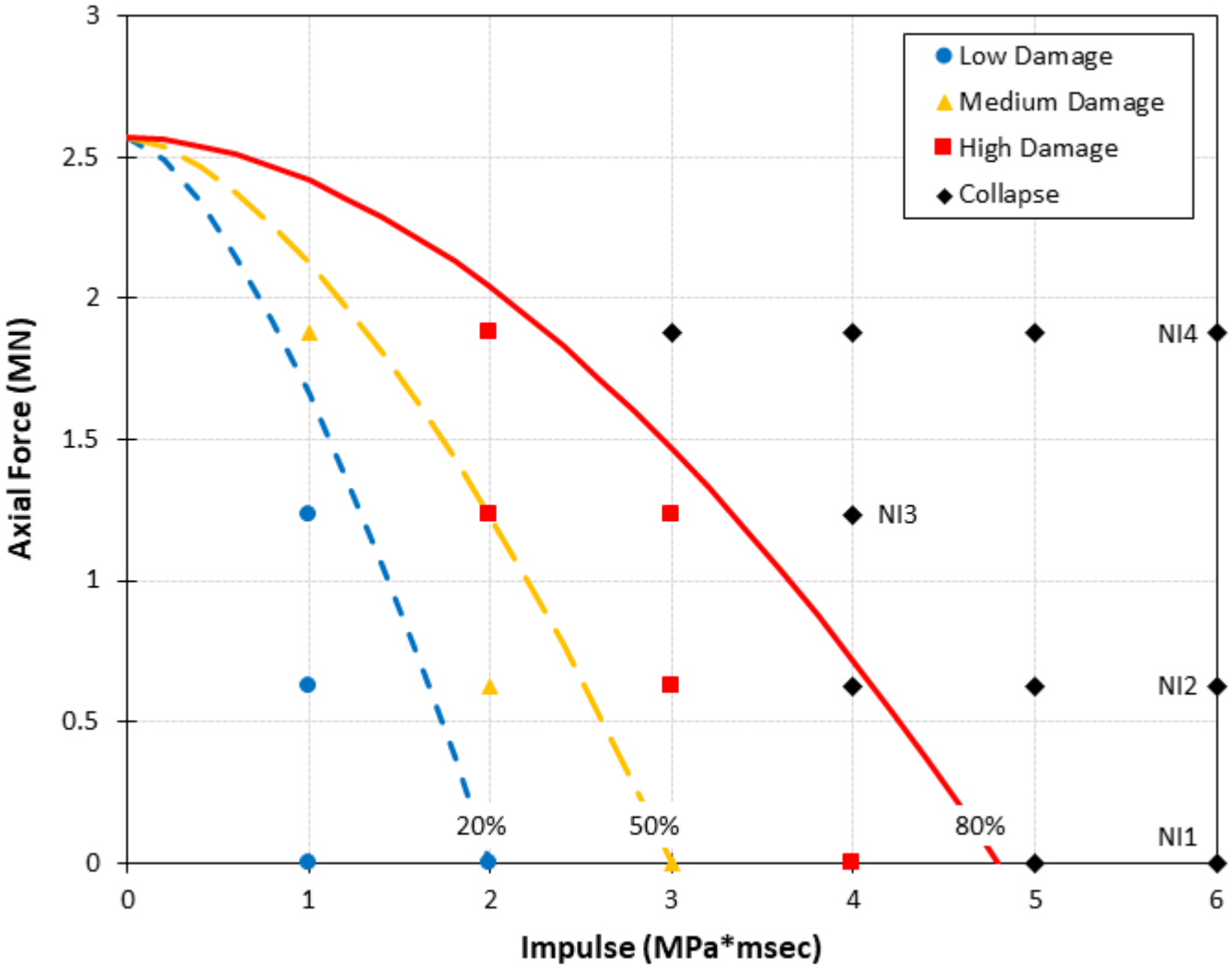

Figure 16. Data sets obtained using NLFEM analyses and N-I curves fitted for 20%, 50% and 80% damage levels.

4.3. Axial Force-Pressure diagrams

Three axial Force-Pressure (N-P) diagrams were also derived using the mixed search algorithm. Four data sets (NP1-4) were generated. The simulation set NP1 corresponds to the axially unloaded column. The axial force increased by ΔN = 625 kN and the peak pressure by ΔP_0 = 0.1 MPa between the simulation sets NP1-4. In all simulations, the duration of the blast load was equal to t_0 = 100 msec to keep the column in

the quasi-static loading regime. The four data sets are presented in Figure 17. Note that the horizontal data set NP1 becomes inclined in Figure 15.

The following dimensionless expression is used to describe the N-P curves

$$\frac{N}{N_{cap}} + \left(\frac{P_0}{A_P}\right)^c = 1 \tag{7}$$

where the exponent c equals 1.2, 1.8 and 2.2 for the 20%, 50% and 80% damage levels, respectively. These c values were obtained by fitting the data sets. The N-P curves derived for low, medium and high damage levels are presented in Figure 17.

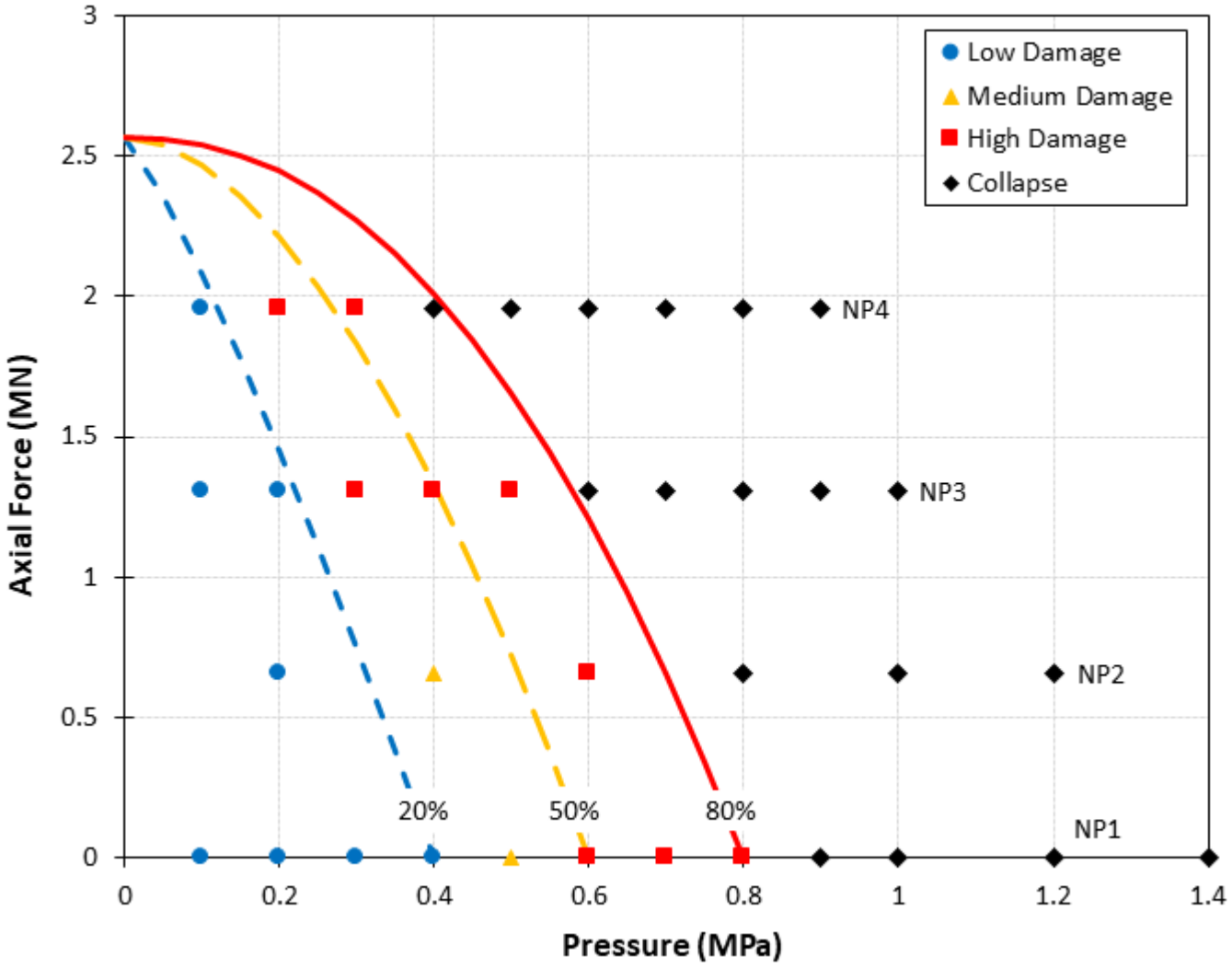

Figure 17. Data sets obtained using NLFEM analyses and N-P curves fitted for 20%, 50% and 80% damage levels.

5. Implementation of extended P-I diagram method

5.1. Dimensional approach

In this section, the extended P-I diagram method is implemented in the dimensional form (see Section 2.1). New P-I diagrams can be obtained using Eqs. (5)-(7) as new P-I expressions or graphically using Figures 15-17. The column loaded by the axial force of N = 1229 kN is used as an example. New diagrams are derived for the 20%, 50% and 80% damage levels. In the first case, A_I and A_P are calculated using Eqs. (6) and (7), respectively, as equal to A_I(20%) = 1.296 MPa·msec, A_I(50%) = 1.997 MPa·msec, A_I(80%) = 3.344 MPa·msec, A_p(20%) = 0.233 MPa, A_p(50%) = 0.418 MPa and A_p(80%) = 0.595 MPa. P-I expressions can be obtained for three damage levels by substituting the A_I and A_P values into Eq. (5), where the values of C_P, C_I and D in Eq. (5) stay the same. Alternatively, expressions for A_I and A_P can be derived from Eqs. (6) and (7) and substituted into Eq. (5). After algebraic manipulations, Eq. (5) can be transformed in a new form of the P-I diagram with a highly nonlinear dependency on the axial force and level of damage, i.e.

$$P_0 I = \frac{\left[C_P \cdot \beta^{-\frac{1}{c}} + C_I \cdot \beta^{-\frac{1}{b}}\right]^D}{\left[1-\beta^{-\frac{1}{c}}\right]\left[1-\beta^{-\frac{1}{b}}\right]} \tag{8}$$

where $\beta = 1 - N/N_{cap}$ represents the effect of the axal force, which indicates that the closer N to N_{cap} the smaller the product $P_0 I$. The constants b and c in Eq. (8) consider the level of damage.

The second case is based on the use of the charts in Figures 15-17. If the P-I expression is not known, new P-I curves can be approximately derived from an existing one by selecting a set of points on the curve, and scaling their coordinates with the factors $A_{I,new}/A_{I,old}$ for the I axis and $A_{P,new}/A_{P,old}$ for the P axis. This process is schematically shown in Figure 2 for a single point B (B_1 transformed to B_2 and B_3). The resulting P-I diagrams derived for the low, medium and high damage levels are presented in Figure 18.

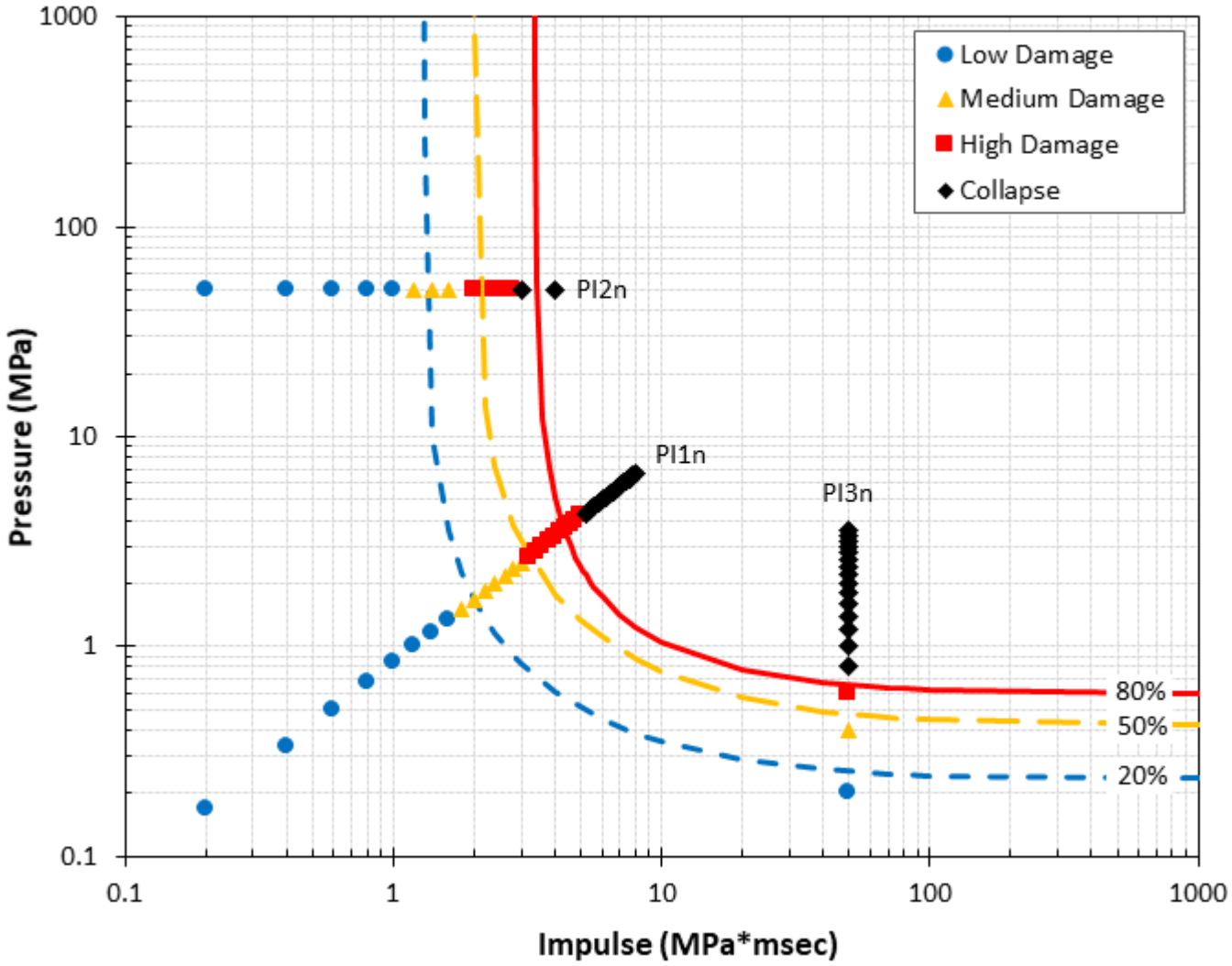

Figure 18. P-I curves derived for axial force of 1229 kN and 20%, 50% and 80% damage levels plotted against new data sets obtained using NLFEM analyses.

In order to verify the new P-I curves, three additional sets of data points were generated using NLFEM analyses of the RC column subjected to N = 1229 kN. The set PI1n was obtained using the mixed search algorithm, the sets PI2n using the pressure-controlled search algorithm, and the set PI3n using the impulse-controlled search algorithm. The new data sets are plotted in Figure 18. It can be observed that the three data sets fall, with some small divergence, into the boundaries defined by the new P-I curves.

The comparison of P-I curves in Figures 7 and 10 shows that the application of the axial force shifts the curves towards the axes, which has also been concluded from the analysis of Eq. (8) in Section 4.3. This shift occurs because the axial force affects the flexural resistance of the column [7, 12]. Similar

observations were made in [50, 60], which showed an increase in damage levels in a RC column with the increase in the axial force.

5.2. Normalised approach

Eq. (5) can be normalised into the following form

$$(p_0 - 1)(i - 1) = (C_P + C_I)^D \quad (9)$$

where $p_0 = P_0/A_P$ and $i = I/A_I$ are the normalised peak pressure and impulse. Given that C_P = 1, C_I = 1 and D = 0.5 (see Section 4.1), the right-hand side of Eq. (1) equals $\sqrt{2}$. The normalised P-I curve is shown in Figure 19. The transformation into the $p_0 - i$ domain eliminates the need for new diagrams. The $p_0 - i$ diagram represents all P-I diagrams that can be derived for the considered RC column subjected to the axial and blast loads. To assess the post-blast loading condition of the RC column, P_0 and I are mapped into the $p_0 - i$ domain using A_P and A_I corresponding to the considered axial force and damage level.

The normalised approach is illustrated using a blast load with P_0 = 1.3 MPa and I = 5.5 MPa·msec. The RC column is first considered as axially unloaded (N = 0 kN) and then as loaded by the axial force of N = 1229 kN. In both cases, the development of 20%, 50% and 80% damage levels is investigated. The mapping of P_0 and I into the $p_0 - i$ domain is done using the corresponding values of A_P and A_I given in Sections 4.1 and 5.1. The $p_0 - i$ data is summarised in Table 1. Figure 19 depicts two sets of three data points generated for the cases considered. In the $p_0 - i$ diagram, the area above the $p_0 - i$ curve corresponds to the situations that occurred, while the area under the curve contains all the situations that did not occur. For example, the data point corresponding to the 20% damage level in the data set of N = 0 kN is located above the $p_0 - i$ curve, while the point corresponding to the 50% damage level is under the curve. This means that the level of damage in the axially unloaded column will be between 20% and 50%.

Table 1. p_0- i data for axial force of 0 kN and 1229 kN and damage level of 20%, 50% and 80%

Damage level	A_I (MPa·msec)	A_P (MPa)	i	p_0
N = 0 kN				
20%	2	0.4	2.750	3.250
50%	3	0.6	1.833	2.167
80%	4.8	0.8	1.146	1.625
N = 1229 kN				
20%	1.296	0.233	4.244	5.579
50%	1.997	0.418	2.754	3.110
80%	3.344	0.595	1.645	2.185

The curves connecting the two sets of data points provide information on the level of damage in the column, which is defined by the intersection of these curves with the $p_0 - i$ curve. To locate the points of intersection accurately, the formulas describing the data sets are required. Alternatively, an approximate estimation of the intersection points can be done using the chart in Figure 19. The regression analysis of the two data sets in Table 1 resulted in the following p_0- i relationships (see Figure 19)

$$p_0 = 0.2456i^2 + 0.0563i + 1.2381 \qquad \text{for } N = 0 \text{ kN} \qquad (10)$$

$$p_0 = 0.3169i^2 - 0.5601i + 2.2488 \qquad \text{for } N = 1229 \text{ kN} \qquad (11)$$

Since the coefficient of determination (R^2) equals 1, a second order polynomial provides a good fit for the data sets. Eq. (9) and Eq. (10) intersect at i = 2.034 and p_0 = 2.368, while Eq. (9) and Eq. (11) intersect at i = 1.967 and p_0 = 2.374. The level of damage can be found approximately by considering a straight line between points on either side of the $p_0 - i$ curve or accurately by interpolating along the curves in Eqs. (10) and (11). This interpolation is based on calculations of curve lengths between two points located on either

side of the $p_0 - i$ curve and the point of intersection with the $p_0 - i$ curve. The length of the curve (s) can be estimated using the following formula

$$s = \int_{i_1}^{i_2} s\sqrt{1 + \left(\frac{dp_0}{di}\right)^2}\, di \tag{12}$$

The application of Eq. (12) to Eqs. (10) and (11) considering the data points in Table 1 and the intersections points results in the 44% damage level in the axially unloaded column and the 72% damage level in the axially loaded column.

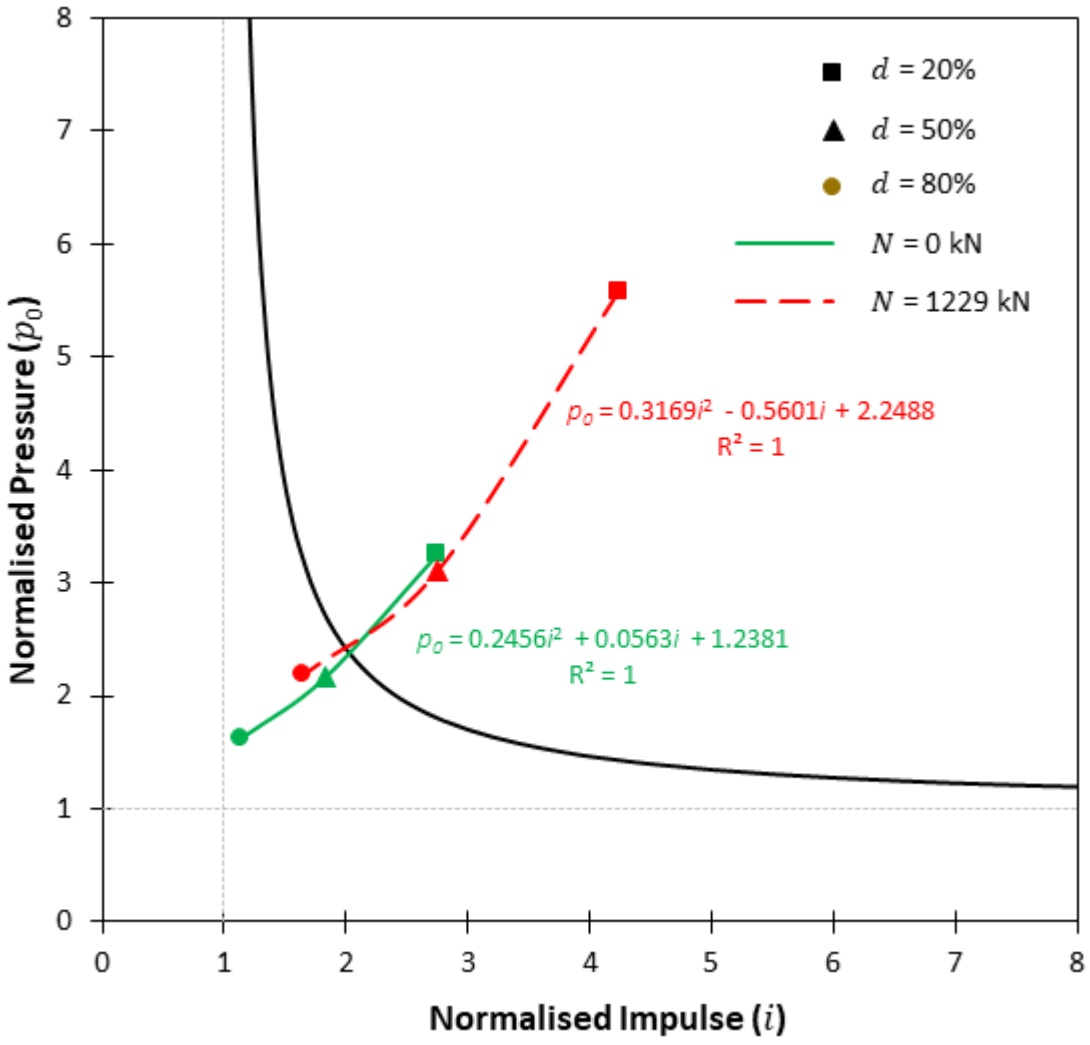

Figure 19. Normalised P-I diagram

In the conventional P-I diagram method the assessment of structural condition of the column (i.e. low, medium and high damage level) loaded by a new axial force would require derivation of 3 new P-I curves

describing 20%, 50% and 80% damage levels, which would involve carrying out at least 3 sets of additional numerical simulations. The additional numerical work is substituted in the normalised extended P-I diagram method with mapping of the blast load onto the normalised P-I diagram using the N-I and N-P relationships, while most of the numerical work has already been done during the derivation of the N-I, N-P and normalised P-I diagrams.

Conclusions

An extended pressure-impulse (P-I) diagram method has been presented in this paper. This method is based on the derivation of a conventional P-I diagram and two complimentary diagrams. The complementary diagrams describe the effects of a structural parameter and the anticipated level of damage on structural response in the impulsive and quasi-static loading regimes, thus defining the positions of P-I curves. The techniques and algorithms necessary for the implementation of this method in dimensional and normalised forms were developed. The extended P-I diagram method was showcased in both forms using a typical reinforced concrete (RC) column subjected to axial and blast loads. The column was modelled in a nonlinear finite element method package – Abaqus. A novel approach was applied to modelling the concrete, which was based on extending the brittle cracking model built-in in Abaqus using user subroutines. The elastic response of this material model in compression was transformed into a nonlinear response of a damaged elasticity model. The new material model was validated at both material and structural levels, demonstrating the ability for realistic description of structural behaviour under a range of loading regimes. Multiple numerical simulations of the RC column subjected to blast load were carried out to derive P-I diagrams for the axially unloaded column and complementary diagrams (i.e. axial force vs. impulse (N-I) and axial force vs. peak pressure (N-P) diagrams) for the axially loaded column. Analytical expressions were found for the P-I, N-I and N-P curves by fitting corresponding data sets. The dimensional and normalised forms of the extended P-I diagram method were demonstrated using these expressions and discussed. It was shown that the dimensional extended P-I diagram method simplifies

derivation of new P-I curves by shifting and scaling an existing curve. The normalised extended P-I diagram method substitutes the derivation of new P-I curves with mapping of new blast loads (characterised by peak pressure and impulse) onto the normalised P-I diagram, which simplifies application framework.

The extended P-I diagram method is graphical in nature and provides visual information on the behaviour of a structural system considered, which is valuable in engineering practice. Therefore, it can be applied in the form of design and assessment charts and can be easily incorporated into relevant standards and design codes.

References

1. Shi, Y., H. Hao, and Z.-X. Li, *Numerical derivation of pressure–impulse diagrams for prediction of RC column damage to blast loads.* International Journal of Impact Engineering, 2008. **35**(11): p. 1213-1227.
2. Krauthammer, T., *Modern Protective Structures*. 2008, Boca Raton: CRC Press.
3. El-Dakhakhni, W., W. Mekky, and S. Changiz-Rezaei, *Vulnerability Screening and Capacity Assessment of Reinforced Concrete Columns Subjected to Blast.* Journal of Performance of Constructed Facilities, 2009. **23**(5): p. 353-365.
4. Ma, G., X. Huang, and J. Li, *Simplified Damage Assessment Method for Buried Structures against External Blast Load.* Journal of Structural Engineering, 2010. **136**(5): p. 603-612.
5. Stolz, A., et al., *Dynamic bearing capacity of ductile concrete plates under blast loading.* International Journal of Impact Engineering, 2014. **69**: p. 25-38.
6. Mutalib, A.A. and H. Hao, *Development of P-I diagrams for FRP strengthened RC columns.* International Journal of Impact Engineering, 2011. **38**(5): p. 290-304.
7. Chernin, L., et al., *Pressure-impulse diagram method - a fundamental review.* Proceedings of the Institution of Civil Engineers-Engineering and Computational Mechanics, 2019. **172**(2): p. 55-69.
8. Command, N.F.E., *Blast Resistant Structures*. 1986.
9. Ambrosini, D., et al., *Location and mass of explosive from structural damage.* Engineering Structures, 2005. **27**(2): p. 167-176.
10. Campidelli, M. and E. Viola, *An analytical–numerical method to analyze single degree of freedom models under airblast loading.* Journal of Sound and Vibration, 2007. **302**(1-2): p. 260-286.
11. Astarlioglu, S., et al., *Behavior of reinforced concrete columns under combined effects of axial and blast-induced transverse loads.* Engineering Structures, 2013. **55**: p. 26-34.
12. Chernin, L., M. Vilnay, and I. Shufrin, *Blast dynamics of beam-columns via analytical approach.* International Journal of Mechanical Sciences, 2016. **106**: p. 331-345.
13. Colombo, M. and P. Martinelli, *Pressure--impulse diagrams for RC and FRC circular plates under blast loads.* European Journal of Environmental and Civil Engineering, 2012. **16**(7): p. 837-862.
14. El-Dakhakhni, W., W. Mekky, and S. Rezaei, *Validity of SDOF Models for Analyzing Two-Way Reinforced Concrete Panels under Blast Loading.* Journal of Performance of Constructed Facilities, 2010. **24**(4): p. 311-325.
15. Huang, X., G.W. Ma, and J.C. Li, *Damage Assessment of Reinfoced Concrete Structural Elements Subjected to Blast Load.* International Journal of Protective Structures, 2010. **1**(1): p. 103-124.
16. Krauthammer, T., et al., *Pressure–impulse diagrams for the behavior assessment of structural components.* International Journal of Impact Engineering, 2008. **35**(8): p. 771-783.
17. Ding, Y., et al., *Damage evaluation of the steel tubular column subjected to explosion and post-explosion fire condition.* Engineering Structures, 2013. **55**: p. 44-55.
18. Fallah, A.S. and L.A. Louca, *Pressure–impulse diagrams for elastic-plastic-hardening and softening single-degree-of-freedom models subjected to blast loading.* International Journal of Impact Engineering, 2007. **34**(4): p. 823-842.
19. Nassr, A.A., et al., *Strength and stability of steel beam columns under blast load.* International Journal of Impact Engineering, 2013. **55**: p. 34-48.
20. Parisi, F., *Blast fragility and performance-based pressure–impulse diagrams of European reinforced concrete columns.* Engineering Structures, 2015. **103**: p. 285-297.
21. Fallah, A.S., E. Nwankwo, and L.A. Louca, *Pressure-Impulse Diagrams for Blast Loaded Continuous Beams Based on Dimensional Analysis.* Journal of Applied Mechanics, 2013. **80**(5): p. 051011.

22. Li, Q. and H. Meng, *Pressure-Impulse Diagram for Blast Loads Based on Dimensional Analysis and Single-Degree-of-Freedom Model.* Journal of Engineering Mechanics, 2002. **128**(1): p. 87-92.
23. Li, Q.M. and H. Meng, *Pulse loading shape effects on pressure–impulse diagram of an elastic–plastic, single-degree-of-freedom structural model.* International Journal of Mechanical Sciences, 2002. **44**: p. 1985-1998.
24. Ma, G.W., H.J. Shi, and D.W. Shu, *P–I diagram method for combined failure modes of rigid-plastic beams.* International Journal of Impact Engineering, 2007. **34**(6): p. 1081-1094.
25. Shi, H.J., H. Salim, and G. Ma, *Using P-I Diagram Method to Assess the Failure Modes of Rigid-Plastic Beams Subjected to Triangular Impulsive Loads.* International Journal of Protective Structures, 2012. **3**(3): p. 333-353.
26. Youngdahl, C., *Correlation parameters for eliminating the effect of pulse shape on dynamic plastic deformation.* Journal of Applied Mechanics, ASME, 1970. **37**(3): p. 744-752.
27. Yu, R.Q., et al., *Non-dimensional pressure-impulse diagrams for blast-loaded reinforced concrete beam columns referred to different failure modes.* Advances in Structural Engineering, 2018. **21**(14): p. 2114-2129.
28. ABAQUS, *Abaqus Version 6.12 Documentation*. 2012, Pawtuchet, RI, USA: Hibbitt, Karlsson & Sorensen, Inc.
29. Vilnay, M., L. Chernin, and D.M. Cotsovos, *Advanced Material Modelling of Concrete in Abaqus*, in *The 9th International Concrete Conference:Environment, Efficiency and Economic Challenges for Concrete*. 2016: Dundee.
30. Mohamed, A.R., M.S. Shoukry, and J.M. Saeed, *Prediction of the behavior of reinforced concrete deep beams with web openings using the finite element method.* Alexandria Engineering Journal, 2014. **53**(2): p. 329-339.
31. Zhang, X., H. Hao, and G. Ma, *Parametric study of laminated glass window response to blast loads.* Engineering Structures, 2013. **56**: p. 1707-1717.
32. Zhu, G., et al., *Estimation of the plastic structural response under impact.* International Journal of Impact Engineering, 1986. **4**(4): p. 271-282.
33. Shi, Y., Z.-X. Li, and H. Hao, *A new method for progressive collapse analysis of RC frames under blast loading.* Engineering Structures, 2010. **32**(6): p. 1691-1703.
34. Huang, X., G.W. Ma, and J.C. Li, *Damage Assessment of Reinforced Concrete Structural Elements Subjected to Blast Load.* International Journal of Protective Structures, 2010. **1**(1): p. 103-124.
35. Abbas, A.A., A.D. Pullen, and D.M. Cotsovos, *Structural response of RC wide beams under low-rate and impact loading.* Magazine of Concrete Research, 2010. **62**(10): p. 723-740.
36. Chen, Y. and I.M. May, *Reinforced concrete members under drop-weight impacts.* Proceedings of the Institution of Civil Engineers-Structures and Buildings, 2009. **162**(1): p. 45-56.
37. Bao, X.L. and B. Li, *Residual strength of blast damaged reinforced concrete columns.* International Journal of Impact Engineering, 2010. **37**(3): p. 295-308.
38. Saatci, S. and F.J. Vecchio, *Effects of Shear Mechanisms on Impact Behavior of Reinforced Concrete Beams.* Aci Structural Journal, 2009. **106**(1): p. 78-86.
39. Sawan, J. and M. Abdel-Rohman, *Impact effect on R.C. slabs: experimental approach.* Journal of Structural Engineering, ASCE, 1986. **112**(9): p. 2057-2065.
40. Wang, W., et al., *Experimental study on scaling the explosion resistance of a one-way square reinforced concrete slab under a close-in blast loading.* International Journal of Impact Engineering, 2012. **49**: p. 158-164.
41. Bhatti, A.Q., et al., *Elasto-plastic impact response analysis of shear-failure-type RC beams with shear rebars.* Materials & Design, 2009. **30**(3): p. 502-510.
42. Cotsovos, D.M. and M.N. Pavlovic, *Modelling of RC beams under impact loading.* Proceedings of the Institution of Civil Engineers-Structures and Buildings, 2012. **165**(2): p. 77-94.

43. Cotsovos, D.M., N.D. Stathopoulos, and C.A. Zeris, *Behavior of RC Beams Subjected to High Rates of Concentrated Loading.* Journal of Structural Engineering-Asce, 2008. **134**(12): p. 1839-1851.
44. Cotsovos, D.M., *A simplified approach for assessing the load-carrying capacity of reinforced concrete beams under concentrated load applied at high rates.* International Journal of Impact Engineering, 2010. **37**(8): p. 907-917.
45. Magnusson, J., M. Halgren, and A. Ansell, *Shear in Concrete Structures Subjected to dynamic Loads.* Structural Concrete, 2014. **15**(1): p. 55-65.
46. Kotsovos, M.D., *Finite-Element Modelling of Structural Concrete: Short-Term Static and Dynamic Loading Conditions*. 2015: CRC Press.
47. Abbas, A.A., S.M.S. Mohsin, and D.M. Cotsovos, *Seismic response of steel fibre reinforced concrete beam-column joints.* Engineering Structures, 2014. **59**: p. 261-283.
48. Hillerborg, A., M. Modéer, and P.-E. Petersson, *Analysis of crack formation and crack growth in concrete by means of fracture mechanics and finite elements.* Cement and Concrete Research, 1976. **6**(6): p. 773-781.
49. fib, *fib Model Code for Concrete Structures 2010*, in *FIB MODEL CODE 2010 O-BK*. 2013, Wiley-VCH Verlag GmbH & Co. KGaA: Weinheim, Germany.
50. Vilnay, M., *Assessing the Behaviour of Reinforced Concrete Columns under Blast Loads*, in *Institute for Infrastructure and Environment*. 2017, Heriot Watt University: Edinburgh. p. 280.
51. Cotsovos, D.M. and M.N. Pavlovic, *Numerical investigation of concrete subjected to compressive impact loading. Part 1: A fundamental explanation for the apparent strength gain at high loading rates.* Computers & Structures, 2008. **86**(1-2): p. 145-163.
52. Cotsovos, D.M. and M.N. Pavlovic, *Numerical investigation of concrete subjected to high rates of uniaxial tensile loading.* International Journal of Impact Engineering, 2008. **35**(5): p. 319-335.
53. Malvar, L.J., et al., *A plasticity concrete material model for DYNA3D.* International Journal of Impact Engineering, 1997. **19**(9-10): p. 847-873.
54. Georgin, J.F. and J.M. Reynouard, *Modeling of structures subjected to impact: concrete behaviour under high strain rate.* Cement & Concrete Composites, 2003. **25**(1): p. 131-143.
55. 3-340-02, U., *Structures to Resist the Effects of Accidental Explosions, Change 2*. 2014, US Army Corps of Engineers: Washington DC.
56. Woodson, S.C. and J.T. Baylot, *Structural collapse: quarter-scale model experiments*. 1999, US Army Corps of Engineers, Engineering Research and Development Center.
57. Rodríguez-Nikl, T., *Experimental simulations of explosive loading on structural components reinforced concrete columns with advanced composite jackets*. 2006, University of California: San Diego.
58. Chen, W.S., H. Hao, and S.Y. Chen, *Numerical analysis of prestressed reinforced concrete beam subjected to blast loading.* Materials & Design, 2015. **65**: p. 662-674.
59. Malvar, L.J., *Review of static and dynamic properties of steel reinforcing bars.* ACI Materials Journal, 1998. **95**(5): p. 609-616.
60. Vilnay, M., D.M. Cotsovos, and L. Chernin, *Numerical investigation of the response of RC columns under blast loads*, in *The 2nd International Conference on Structural Safety under Fire & Blast, CONFAB2017*. 2017: London, UK.